

# Global Properties of the Rich Cluster ABCG 209 at z~0.2. Spectroscopic and Photometric Catalogue<sup>\*†</sup>

A. Mercurio<sup>1</sup>, F. La Barbera<sup>1</sup>, C. P. Haines<sup>1,2</sup>, P. Merluzzi<sup>1</sup>, G. Busarello<sup>1</sup>  
and M. Capaccioli<sup>3,4</sup>

<sup>1</sup>*INAF-Osservatorio Astronomico di Capodimonte, I-80131 Napoli*

<sup>2</sup>*School of Physics and Astronomy, University of Birmingham, Edgbaston, Birmingham, B15 2TT, UK*

<sup>3</sup>*Dipartimento di fisica, Università ‘Federico II’ di Napoli, I-80126 Napoli*

<sup>4</sup>*INAF-VSTCen, I-80131 Napoli*

Released 2006 XXXXX XX

## ABSTRACT

This paper is aimed at giving an overview of the global properties of the rich cluster of galaxies ABCG 209. This is achieved by complementing the already available data with new medium resolution spectroscopy and NIR photometry which allow us to i) analyse in detail the cluster dynamics, distinguishing among galaxies belonging to different substructures and deriving their individual velocity distributions, using a total sample of 148 galaxies in the cluster region, of which 134 belonging to the cluster; ii) derive the cluster NIR luminosity function; iii) study the Kormendy relation and the photometric plane of cluster early-type galaxies (ETGs). Finally we provide an extensive photometric (optical and NIR) and spectroscopic dataset for such a complex system to be used in further analyses investigating the nature, formation and evolution of rich clusters of galaxies.

The present study shows that the cluster is characterised by a very high value of the line-of-sight velocity dispersion:  $\sigma_v = 1268_{-84}^{+93}$  km s<sup>-1</sup>, that results in a virial mass of  $M_{vir} = 2.95_{-0.78}^{+0.80} \times 10^{15}$  h<sub>70</sub><sup>-1</sup> M<sub>⊙</sub> within  $R_{vir} = 3.42 h_{70}^{-1}$  Mpc. The analysis of the velocity dispersion profile shows that such high value of  $\sigma_v$  is already reached in the central cluster region. There is evidence

<sup>\*</sup> Based on observations collected at European Southern Observatory (ESO ObsID.s 068.A-0116, 074.A-0073 and 075.A-0845) and at the Telescopio Nazionale Galileo (TNG ObsID AOT12/TAC-07).

of three significant substructures, the primary one having a velocity dispersion of  $\sigma_v = 847^{+52}_{-49} \text{ km s}^{-1}$ , which makes it consistent with mass estimates from weak lensing analyses.

This observational scenario confirms that ABCG 209 is presently undergoing strong dynamical evolution with the merging of two or more subclumps. This interpretation is also supported by the detection of a radio halo (Giavannini et al. 2006) suggesting that there is a recent or ongoing merging.

Cluster ETGs follow a Kormendy relation whose slope is consistent with previous studies both at optical and NIR wavelengths. We investigate the origin of the intrinsic scatter of the photometric plane due to trends of stellar populations, using line indices as indicators of age, metallicity and  $\alpha/\text{Fe}$  enhancement. We find that the chemical evolution of galaxies could be responsible for the intrinsic dispersion of the Photometric Plane.

**Key words:** galaxies: clusters: general - galaxies: clusters: individual: ABCG 209 - galaxies: distances and redshifts - galaxies: kinematics and dynamics - galaxies: photometry - galaxies: luminosity function

## 1 INTRODUCTION

Galaxy clusters are complex systems involving a variety of interacting components: galaxies, hot and cold gas, dark matter. Among them, about 50% are unrelaxed systems (Smith et al. 2005) and a large fraction contain substructures (e.g., Girardi et al. 2006 and references therein), suggesting that they are evolving via merging processes from poor groups to rich structures. In fact, in hierarchical clustering cosmological scenarios, galaxy clusters form from the accretion of subunits. Numerical simulations show that clusters form preferentially through the anisotropic accretion of subclusters along filaments (e.g., Colberg et al. 1999, Diaferio et al. 2001).

Detailed multi-band studies of such systems are crucial to probe structure formation scenarios as well as to investigate galaxy evolution processes. ABCG 209 is an ideal target for such a study, since it is a rich (richness class  $R = 3$ ; Abell et al. 1989), X-ray luminous ( $L_X(0.1\text{--}2.4\text{ keV}) \sim 2.7 \times 10^{45} h_{70}^{-2} \text{ erg s}^{-1}$ , Ebeling et al. 1996;  $T_X \sim 10 \text{ keV}$ , Rizza et al. 1998), and massive cluster ( $M(R < R_{\text{vir}}) = 2.3\text{--}3.1 \times 10^{15} h_{70}^{-1} M_\odot$  Mercurio et al. 2003a, Paulin-Henriksson et al. 2007). Evidence for a complex dynamical status comes from the

† Tables 2 and 3 are available only in electronic format.

X-ray emission: the hot gas is elongated and distributed asymmetrically showing two main clumps (Rizza et al. 1998). However no strong cooling flow is detected. Moreover, the young dynamical state is indicated by the possible presence of a radio halo (Giovannini et al. 1999, 2006), which has been suggested to be the result of a recent cluster merger, through the acceleration of relativistic particles by the merger shocks (Feretti 2002, 2007).

Dynamical properties of the cluster were analysed through a spectroscopic survey of 112 cluster members (Mercurio et al. 2003a) and photometric properties of the cluster galaxies were derived out to radii of 3-4  $h_{70}^{-1}$  Mpc, taking advantage of wide field CFHT  $B$ - and  $R$ -band images (Haines et al. 2004). Our analyses (Mercurio et al. 2003a, 2003b, 2004; La Barbera et al. 2003a, 2003b, 2004; Haines et al. 2004) showed that ABCG 209 has a very complex structure, with: **a)** a high value of the line-of-sight velocity dispersion, with  $\sigma_v = 1394^{+88}_{-99} \text{ km s}^{-1}$ ; **b)** a significantly non-Gaussian redshift distribution, and a velocity gradient (and elongation of the cD galaxy) in the SE-NW direction; **c)** the presence of substructures in the X-ray emission; **d)** the presence of a merger clump observed 1-2 Gyr after the merging; **e)** a strong spatial and spectral segregation of galaxies, with (i) young blue emission line galaxies uniformly distributed in the low density regions, (ii) blue post-starburst galaxies aligned in a direction perpendicular to the cluster elongation, and (iii) red post-starburst galaxies and early type galaxies distributed along the cluster elongation. Moreover, we have examined the effect of cluster environment, as measured in terms of the local surface density of  $R < 23.0$  mag galaxies, on the global properties of the cluster galaxies, through their luminosity functions, colour-magnitude relations, and average colours. The LFs for galaxies within the virialized region are found to be well described by single Schechter functions, although there is an indication of a dip at  $R=20\text{-}20.5$  mag. The faint-end slope shows a strong dependence on environment, becoming steeper at more than  $3\sigma$  significance level from high- to low-density environments. We explain this trend as a combination of the morphology-density relation and dwarf galaxies being cannibalised and disrupted by the cD galaxy and interactions with the intra-cluster medium in the cluster core.

Our weak lensing analysis (Paulin-Henriksson et al. 2007) confirms that ABCG 209 is a massive cluster, although the mass estimated by weak lensing ( $M(R < R_{200}) = 7.7^{+4.3}_{-2.7} \times 10^{14} h_{70}^{-1} M_\odot$ ) is lower than that obtained by Mercurio et al. (2003a) from the analysis of the dynamical properties. The centres of the X-ray emission, dark matter and galaxy distributions all appear offset from one another, with the centre of mass found from the weak lensing analysis lying between that of the X-ray and galaxy distributions, with all three centres of

mass aligned on the main SE-NW axis of the cluster (see Figs. 6 and 7 of Paulin-Henriksson et al. 2007). Such an effect is seen for the more extreme “Bullet cluster” (Clowe et al. 2004), and seems to reflect the different responses of the gas and dark matter components to the merger, in agreement with the merging scenario for ABCG 209.

The above results show that it is crucial to relate the properties of member galaxies to the global properties of clusters, such as mass and dynamical state. The spatial and kinematical analysis of member galaxies allows to detect and measure the amount of substructure and to identify and analyse possible pre-merging clumps or merger remnants. In addition, sub-clustering is important for processes of galaxy evolution. In fact, although the high galaxy velocity dispersion associated with a relaxed, virialized clusters inhibits galaxy mergers, in subclusters, where the velocity dispersions are lower, such mergers are more probable and could have an important role in building elliptical galaxies (see Moss 2006).

Identifying substructures is difficult with galaxy positions alone, since projected distribution of galaxy clusters could show clumps that are not real. The optical spectroscopy of member galaxies is the most reliable tool to investigate these clumps and allows us to study the dynamics of cluster mergers, since it provides direct information on the velocity field. However, this is often an arduous investigation due to the limited number of galaxies usually available to trace the velocity field.

In order to achieve the resolution needed to understand the complex dynamics of ABCG 209 and to investigate the environmental effects on galaxy evolution, we complement the previously described dataset with medium resolution spectra analysing a total sample of 148 galaxies in the cluster region. The enlarged data sets allow us to better distinguish among galaxies belonging to different substructures and to derive their individual velocity distributions. A detailed study of substructures is also important to investigate the reason for the discrepancy between lensing and dynamical mass estimates. We also present new *K*-band observations, that allow us to derive the cluster NIR luminosity function (LF) and are directly related to the galaxy mass function. Additionally, at infrared wavelengths the galaxy luminosities do not depend strongly on the details of their stellar populations (Gavazzi, Pierini, & Boselli 1996).

In this paper we provide the spectroscopic catalogue of the new targets and a photometric catalogue with measured photometric redshifts, *B*-, *V*-, *R*- and *K*-band total magnitudes and spectroscopic redshifts when available. We also derive structural parameters of cluster galaxies, selected according to the photometric and spectroscopic redshifts; and we

investigate the photometric correlations of ETGs, such as the mean surface brightness-size relation, also known as the kormendy relation (KR; Kormendy 1977) and the Photometric Plane (PHP; La Barbera et al. 2005).

The paper is organised as follows. We present the new data in Sect. 2 and we derive photometric and spectroscopic redshifts in Sect. 3 where the catalogue of the cluster members is also described. We analyse the global cluster properties in Sect. 4 and the internal dynamics and substructures in Sect. 5. We describe the derivation of structural properties of ETGs in Sect. 6, deriving also the KR and the PHP. Finally we discuss and summarise our results in Sect. 7.

Unless otherwise stated, we give errors at the 68% confidence level (hereafter c.l.). Throughout the paper, we assume a flat cosmology with  $\Omega_m = 0.3$ ,  $\Omega_\Lambda = 0.7$ , and  $H_0 = 70 \text{ km s}^{-1} \text{ Mpc}^{-1}$ . For this cosmological model,  $1'$  corresponds to 271 kpc at the cluster redshift.

## 2 OBSERVATIONS AND DATA REDUCTION

Spectroscopic observations were carried out at the ESO New Technology Telescope (NTT) with the ESO Multi Mode Instrument (EMMI) and at the Telescopio Nazionale Galileo (TNG) with the Device Optimized for the LOw RESolution (DOLORES), while NIR photometric data were collected with the Son OF ISAAC (SOFI) at NTT.

### 2.1 Photometry

New  $K$ -band images for the cluster of galaxies ABCG 209 were collected with SOFI operating in the LARGE FIELD observing mode, providing a field of view of  $5' \times 5'$  with a pixel scale of  $0.288''/\text{pxl}$ . Eight overlapping fields were observed, each of them with a dithered sequence of 36 exposures. We adopted a  $20''$  dithering box, with DIT and NDIT values of 6 s and 10, respectively. This resulted in an integration time of 60s for each exposure, and a total integration time of 2160s for each field. Sky conditions were photometric during five out of six observing nights. During those nights we observed standard stars from the list of Persson et al. (1998), at five different positions on the chip.

The data were reduced using FORTRAN routines developed by the authors. For each dithering sequence, the exposures were dark subtracted and flat-field corrected, using a superflat frame obtained by median combining all the images taken during a given night. After this procedure, the magnitudes of the standard stars showed a rms variation across

the chip of  $\sim 0.05$  mag. To achieve a better accuracy, we retrieved  $K$ -band images from the ESO archive for a standard star observed at different positions in a  $5 \times 5$  grid on the SOFI frame. We chose standard star observations as close as possible in time to those of ABCG 209. Illumination correction frames were then obtained for each night by measuring the magnitude of the standard star as a function of the position on the frame. This allowed the low spatial frequency component of the flat-field to be corrected to better than 1%. Since sky subtraction is a very troublesome step for the reduction of NIR data, particularly in high density regions, this point was carefully dealt with by a two step procedure. First, each exposure was sky subtracted by computing the sky frame from the median of the six closest frames along the sequence. The images were then registered with integer shifts and combined using a sigma clipping algorithm for cosmic ray rejection. This procedure alone overestimates the sky level in the extended halos of galaxies. To minimise this effect, we reiterated the sky subtraction as follows. The initial combined images were used to obtain mask frames for the sources in the field, by running SExtractor with the checkimage OBJECTS option. For each sequence, the mask was expanded in order to 'cover' the galaxy halos and was de-registered to each dithered exposure. The hot and bad pixels were also masked. The sky frames were estimated as the average of the six closest frames to the exposures from that sequence, rejecting masked pixels. The exposures of each dithering sequence were then sky subtracted and combined with the IRAF<sup>1</sup> task IMCOMBINE. The images of the different fields were combined by taking into account their different zero-points, resulting in a final  $K$ -band mosaic with an average seeing FWHM of  $\sim 0.8''$ . The mosaic is shown in Fig. 1.

The photometric calibration was performed for the  $K_s$  standard filter (Persson et al. 1998), deriving the instrumental magnitudes of the standard stars within an aperture of  $8''$  diameter. The airmass correction was performed by using an extinction coefficient  $A_K = 0.05$  mag/airmass, which was derived by comparing the magnitudes of bright objects in the field for different airmasses. The typical accuracy on the zero-point of each photometric night amounts to  $\sim 0.01$  mag. The images of the different fields were normalised to the average zero-point value of 22.425 (scaled to 1 s exposure time).

<sup>1</sup> IRAF is distributed by the National Optical Astronomy Observatories, which are operated by the Association of Universities for Research in Astronomy, Inc., under cooperative agreement with the National Science Foundation.

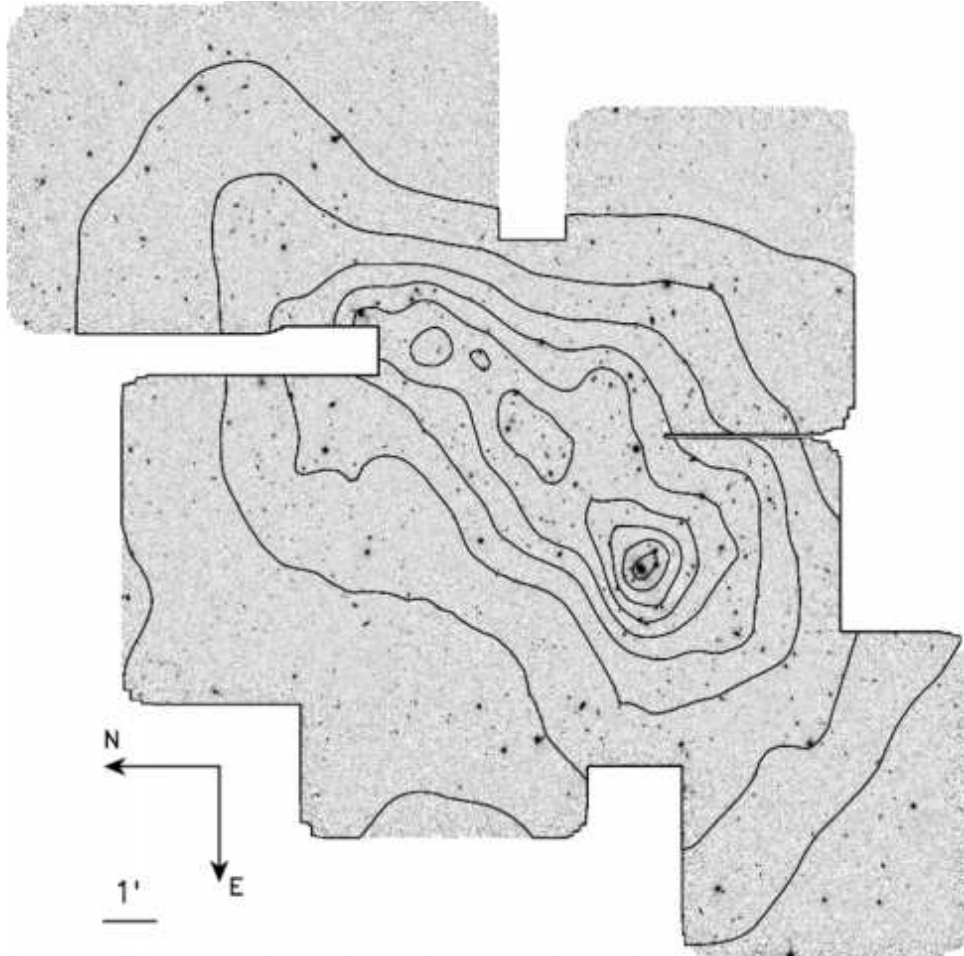


**Figure 1.** K-band mosaic image of ABCG 209. Contours are obtained from the projected number density map of  $K < 17.5$  mag galaxies. The contour density values are equally spaced by 1.27 galaxies  $\text{arcmin}^{-2}$ , with the outermost and innermost contours corresponding to surface density values of 1.4 galaxies  $\text{arcmin}^{-2}$  and 9 galaxies  $\text{arcmin}^{-2}$ , respectively. The mosaic covers an area of  $\sim 0.0525$  square degrees, corresponding to  $\sim 1.39 h_{70}^{-2} \text{ Mpc}^2$  at  $z=0.209$ .

## 2.2 Spectroscopy

The spectroscopic data were obtained with the multi-object spectroscopy (MOS) mode. Targets were selected according to the  $B-R$  vs.  $R$  colour-magnitude relation (CM). We gave priority to the galaxies lying on the CM relation up to  $R=20.0$  mag. We acquired one mask with EMMI (field of view  $5' \times 8.6'$ ), centred on  $\alpha_{J2000} = 01:31:53.0$ ,  $\delta_{J2000} = -13:37:42.8$ , allocating 28 slits and one with DOLORES (field of view  $6' \times 7.7'$ ), centred on  $\alpha_{J2000} = 01:31:52.0$ ,  $\delta_{J2000} = -13:37:30.8$ , allocating 33 slits. We integrated for 8100 sec

with EMMI-Grism#5 yielding a dispersion of  $\sim 1.6$  Å/pxl (resolution= $\sim 4.8$  Å FWHM) in the spectral range 380-702 nm, and for 16200 sec with DOLORES-grism MR-B, giving a dispersion  $\sim 1.9$  Å/pxl (resolution= $\sim 4.2$  Å FWHM) in the spectral range 350-700 nm.

Each scientific exposure (as well as flat fields and calibration lamps) was bias subtracted. The individual spectra were extracted and flat field corrected. Cosmic rays were rejected in two steps. First, we removed the cosmic rays lying close to the objects by interpolation between adjacent pixels, then we combined the different exposures by using the IRAF task IMCOMBINE with the algorithm CRREJECT (the positions of the objects in different exposures were checked before). Wavelength calibration was obtained using He-Ar and He lamp spectra for EMMI and DOLORES, respectively. The typical rms scatter around the dispersion relation was  $\sim 8$  km s $^{-1}$  and 11 km s $^{-1}$  for EMMI and DOLORES respectively.

The positions of the objects in the slits were defined interactively using the IRAF package APEXTRACT. The exact object position within the slit was traced in the dispersion direction and fitted with a low order polynomial to allow for atmospheric refraction. The spectra were then sky subtracted and the rows containing the object were averaged to produce the one-dimensional spectra. The signal-to-noise ratio per pixel of the one-dimensional galaxy spectra belonging to the cluster ranges from about 6 to 18 in the region around the Mg line (at 625 nm in the spectra at  $z\sim 0.2$ ) for EMMI spectra and from about 8 to 27 for the spectra obtained with DOLORES.

### 3 REDSHIFT MEASUREMENTS

#### 3.1 Spectroscopic redshifts

Redshifts were derived using the cross-correlation technique (Tonry & Davis 1981), as implemented in the RVSAO package. We adopted galaxy spectral templates from Kennicutt (1992), corresponding to morphological types E, S0, Sa, Sb, Sc and Ir. The correlation was computed in the Fourier domain. We define the redshift as the value given by the *best template spectra*, i.e. the template producing the highest value of the correlation *R-value* given by RVSAO that gives an indication of the signal-to-noise of the correlation peak.

Of the 61 observed spectra, 44 turned out to be at the redshift of ABCG 209, 1 is a foreground galaxy and 6 are background galaxies. In 10 cases we could not determine the redshift. In Table 1 we report spectroscopic redshift measurements of the observed galaxies.

In order to estimate the uncertainties in the redshift measurements, we considered the

**Table 1.** Spectroscopic data. Running number for galaxies in the present sample, right ascension and declination (Col. 1, Col. 2); heliocentric corrected redshift z (Col. 3).

$\alpha$	$\delta$	z
01 31 45.33	-13 41 53.0	0.2004 ± 0.0004
01 31 56.81	-13 41 31.7	0.2182 ± 0.0002
01 31 47.02	-13 41 17.9	0.2030 ± 0.0002
01 31 48.41	-13 41 00.4	0.2079 ± 0.0002
01 31 45.78	-13 40 37.8	0.2031 ± 0.0002
01 32 01.00	-13 40 17.5	0.2113 ± 0.0003
01 31 52.41	-13 40 02.0	0.1989 ± 0.0003
01 31 42.47	-13 39 44.3	0.2539 ± 0.0003 <sup>a</sup>
01 32 01.27	-13 39 33.3	0.2103 ± 0.0005
01 31 57.49	-13 39 23.4	0.2165 ± 0.0003
01 31 47.06	-13 39 06.7	0.3116 ± 0.0003 <sup>a</sup>
01 31 45.35	-13 38 46.0	0.2522 ± 0.0003 <sup>a</sup>
01 31 46.73	-13 38 29.2	0.2519 ± 0.0003 <sup>a</sup>
01 31 52.37	-13 37 40.6	0.1980 ± 0.0002
01 31 52.91	-13 37 34.6	0.2150 ± 0.0002
01 31 56.40	-13 37 18.3	0.2080 ± 0.0003
01 31 51.79	-13 36 54.8	0.2074 ± 0.0002
01 31 53.25	-13 36 44.2	0.2098 ± 0.0004
01 31 52.52	-13 36 27.5	0.2110 ± 0.0003
01 31 42.34	-13 36 06.4	0.2080 ± 0.0003
01 32 04.29	-13 35 57.0	0.3702 ± 0.0005 <sup>a</sup>
01 31 49.42	-13 35 44.5	0.2164 ± 0.0004
01 31 44.94	-13 35 11.3	0.2130 ± 0.0002
01 31 49.39	-13 34 59.3	0.2078 ± 0.0003
01 31 49.14	-13 34 45.5	0.4025 ± 0.0002 <sup>a</sup>
01 31 48.95	-13 34 34.9	0.2058 ± 0.0005
01 31 48.33	-13 34 23.5	0.1486 ± 0.0004 <sup>b</sup>
01 31 43.11	-13 34 07.5	0.2109 ± 0.0002
01 31 40.63	-13 33 46.3	0.2097 ± 0.0003

<sup>a</sup> Background galaxy.

<sup>b</sup> Foreground galaxy.

error calculated with the cross-correlation technique, which is based on the width of the peak and on the amplitude of the antisymmetric noise from the cross correlation (cf. manual of the XCSAO task). The wavelength calibration errors (see Sect. 2.1) turned out to be negligible in this respect. The errors derived from the cross-correlation could however be smaller than the true errors (e.g. Boschin et al. 2006 and references therein). We checked the error estimates by comparing redshifts computed for 17 galaxies observed with EMMI and 5 with DOLORES which were already acquired in a previous observation carried out with EMMI (Mercurio et al. 2003a). The two data sets agree with a one-to-one relation, and a reasonable value of  $\chi^2$  for the fit, in particular for the spectra acquired with DOLORES, was obtained when the errors derived from the cross-correlation were multiplied by a correction factor  $\sim 1.5$ . A similar correction was obtained by Malumuth et al. (1992; 1.6), Bardelli et al. (1994; 1.87), and Quintana et al. (2000; 1.57). Since we are comparing redshifts measured from spectra acquired in different periods and with different instruments, the multiplicative factor obtained through this comparison takes also into account possible external errors.

### 3.2 Photometric redshifts

The redshifts of galaxies without spectroscopic information were estimated by means of the photometric redshift technique, using a similar approach to that described in Busarello et al. (2002) and La Barbera et al. (2003c). Photometric redshifts were estimated according to the Spectral Energy Distribution fitting method (see Massarotti et al. 2001a,b, and references therein), using the new  $K$ -band photometry, as well as the already published  $B$ -,  $V$ -, and  $R$ -band photometry of ABCG 209. The  $B$ - and  $R$ -band data, described in Haines et al. 2004, are available on the entire field covered by the new  $K$ -band photometry, while the  $V$ -band imaging (see Mercurio et al. 2003b) covers a smaller region of  $\sim 160$  arcmin $^2$  centred around the cluster core. Photometry of sources in the  $K$ -band mosaic are obtained by means of SExtractor (Bertin & Arnouts 1996), as detailed in Sec. 4.1.1. Galaxy colours were measured within an aperture of 5'' diameter. Since all the  $BVRK$  images have similar seeing FWHM values (0.7'' – 0.9''), no aperture corrections were applied to galaxy colours.

Photometric redshifts were measured for the 642 galaxies, with available photometry in  $B$ ,  $R$ , and  $K$  bands, brighter than  $R = 21$  mag: the magnitude limit for spectroscopic observation. We looked for redshifts in the range  $z \in [0.0, 1.0]$  with a step of 0.01, imposing that at a given redshift galaxy templates would be younger than the age of the universe in the adopted cosmology. We used the GISSEL03 spectral code (Bruzual & Charlot 2003) to produce galaxy templates with a Scalo IMF and an exponential SFR,  $e^{-t/\tau}$ . The colours of E/S0, Sa/Sb, and Sc/Sd spectra were modelled by choosing  $\tau = 1, 4$  and 15 Gyr, respectively, while early-type galaxies with different metallicities were described by using E/S0 models with  $Z/Z_{\odot} = 0.2, 0.4, 1$  and 2.5. The differential dust extinction of the Milky Way was included in the computation of model colours by adopting the extinction curve of Cardelli, Clayton and Mathis (1989) and a colour excess of  $E(B - V) = 0.019$  (Schlegel, Finkbeiner and Davis 1998). The uncertainty on the photometric redshift,  $\delta z$ , was estimated by performing numerical simulations, shifting galaxy colours according to their corresponding uncertainties, and recomputing each time the photometric redshifts.

We compared photometric and spectroscopic redshifts for  $N = 134$  galaxies in the cluster field. We found that galaxies with large relative uncertainties on photometric redshifts were biased toward higher redshift values. In order to reduce this systematic effect, we removed from the sample those galaxies with a value of  $\delta z / (1 + z)$  larger than 0.07. This selection leads to a sample of 399 (out of 642) galaxies with reliable photometric redshift estimates (see

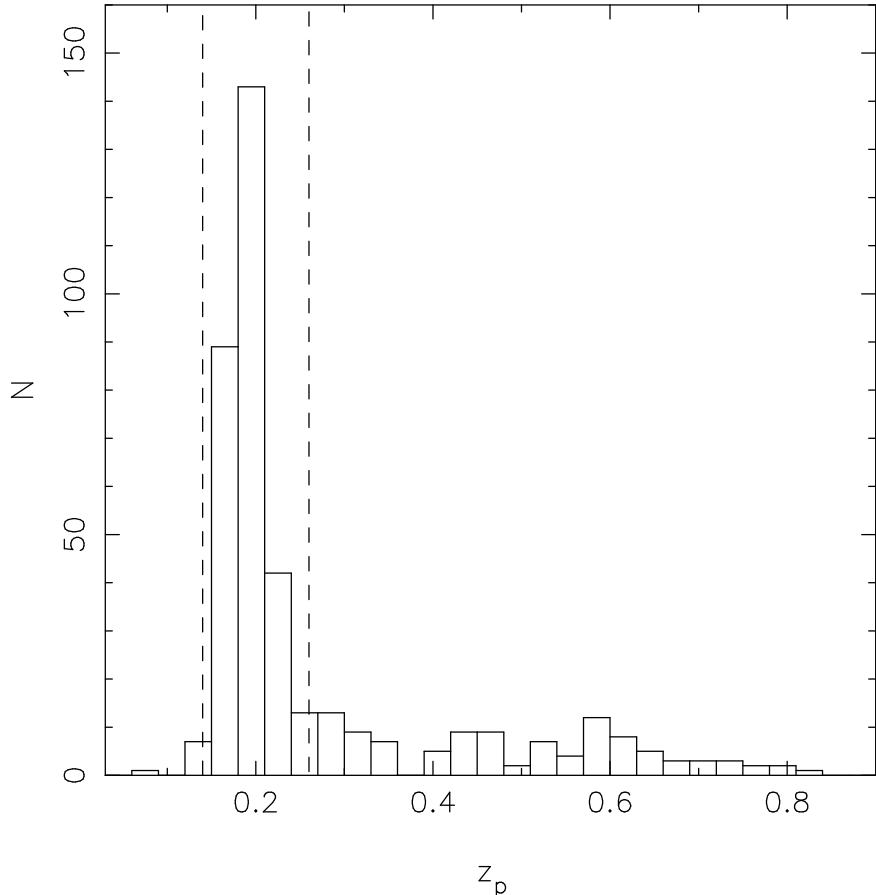


**Figure 2.** Distribution of photometric redshifts for galaxies with a relative uncertainty on photometric redshifts smaller than 0.07. The dashed lines mark the redshift range that defines likely cluster members.

Table 2). As shown in Fig. 2, the distribution of these photometric redshifts is dominated by the peak around  $z \sim 0.2$ , indicating that most galaxies with  $R \leq 21$  in the  $K$ -band field are actually cluster members. After comparison with spectroscopic redshifts, we chose to mark as likely cluster members those galaxies in the photometric redshift range of 0.14 to 0.26. This selection leads to a sample of 292 (out of 399) galaxies which are likely cluster members.

### 3.3 Catalogues

The new spectroscopic catalogue is presented in Table 1, which contains the sky coordinates  $\alpha$  (Col. 1) and  $\delta$  (Col. 2), and the spectroscopic redshift (Col. 3).

The catalogue of galaxies with reliable photometric redshifts ( $\delta z/1 + z < 0.07$ ) is presented in Table 2, available in electronic format, which includes the identification number of each galaxy, ID (Col. 1), right ascension and declination (J2000),  $\alpha$  and  $\delta$  (Cols. 2 and 3),  $B$  (Col. 4),  $V$  (Col. 5) and  $R$  magnitudes when available (Col. 6),  $K$  magnitudes (Col. 7),

**Table 2.** Photometric data. Running number for galaxies in the present sample, ID (Col. 1); right ascension and declination (Col. 2, Col. 3) B-, V-, R- and K-band Kron magnitude (Col. 4, Col. 5, Col. 6, Col. 7); heliocentric corrected redshift z (Col. 8); photometric redshift (Col. 7).

ID	$\alpha$	$\delta$	B	V	R	K	$z_{\text{spec}}$	$z_{\text{phot}}$
1	01 31 47.23	-13 35 31.2	21.97 ± 0.02	20.35 ± 0.03	19.73 ± 0.01	17.06 ± 0.02	...	0.155
2	01 31 49.46	-13 37 26.9	19.12 ± 0.01	18.02 ± 0.02	17.57 ± 0.01	15.11 ± 0.01	0.2140 ± 0.0002	0.170
3	01 31 55.10	-13 37 24.1	21.92 ± 0.01	21.27 ± 0.03	20.63 ± 0.01	18.71 ± 0.09	...	0.451
4	01 31 55.68	-13 37 19.9	23.09 ± 0.03	21.43 ± 0.03	20.94 ± 0.01	18.18 ± 0.07	...	0.147
5	01 31 51.56	-13 37 18.0	22.03 ± 0.02	20.46 ± 0.02	19.67 ± 0.01	16.54 ± 0.01	...	0.209
6	01 31 51.28	-13 37 17.5	22.54 ± 0.02	21.06 ± 0.02	20.34 ± 0.01	17.47 ± 0.03	...	0.160
7	01 31 56.40	-13 37 18.2	22.17 ± 0.02	20.65 ± 0.02	19.97 ± 0.01	16.93 ± 0.02	0.2080 ± 0.0003	0.155
8	01 31 54.59	-13 37 04.3	22.56 ± 0.03	19.95 ± 0.03	20.38 ± 0.01	17.27 ± 0.03	...	0.145
9	01 31 55.12	-13 37 04.7	20.96 ± 0.01	18.93 ± 0.02	18.58 ± 0.01	15.36 ± 0.01	0.2118 ± 0.0003	0.242
10	01 31 55.18	-13 36 57.9	20.74 ± 0.01	18.94 ± 0.02	18.40 ± 0.01	15.25 ± 0.01	0.2150 ± 0.0002	0.186
11	01 31 51.07	-13 36 27.6	22.96 ± 0.03	20.49 ± 0.03	20.78 ± 0.01	17.91 ± 0.05	...	0.145
12	01 31 52.29	-13 36 58.3	19.53 ± 0.01	17.37 ± 0.02	17.19 ± 0.01	14.14 ± 0.00	0.2024 ± 0.0002	0.186
13	01 31 51.79	-13 36 54.8	22.09 ± 0.02	20.20 ± 0.02	19.88 ± 0.01	16.58 ± 0.02	0.2074 ± 0.0002	0.155
14	01 31 52.52	-13 36 27.5	21.54 ± 0.01	18.39 ± 0.02	19.33 ± 0.01	14.90 ± 0.02	0.2110 ± 0.0003	0.209
15	01 31 53.25	-13 36 44.2	22.78 ± 0.03	19.50 ± 0.02	19.92 ± 0.01	16.06 ± 0.06	0.2098 ± 0.0004	0.165
16	01 31 52.87	-13 36 35.2	21.51 ± 0.02	19.79 ± 0.02	19.28 ± 0.01	16.29 ± 0.04	...	0.145
17	01 31 52.57	-13 36 44.2	21.35 ± 0.01	19.38 ± 0.02	18.75 ± 0.01	15.66 ± 0.01	...	0.170
18	01 31 52.53	-13 36 40.5	18.76 ± 0.01	17.00 ± 0.02	16.41 ± 0.01	12.77 ± 0.00	0.2097 ± 0.0002	0.222
19	01 31 50.97	-13 36 49.6	21.27 ± 0.01	19.64 ± 0.02	19.06 ± 0.01	16.12 ± 0.01	0.2042 ± 0.0003	0.155
20	01 31 56.22	-13 36 46.8	20.16 ± 0.01	18.43 ± 0.02	18.10 ± 0.01	15.19 ± 0.01	0.2098 ± 0.0003	0.150
21	01 31 48.64	-13 36 46.6	22.76 ± 0.03	21.36 ± 0.03	20.58 ± 0.01	17.63 ± 0.03	...	0.180
22	01 31 51.32	-13 36 56.8	19.84 ± 0.01	18.10 ± 0.02	17.49 ± 0.01	14.35 ± 0.00	0.2068 ± 0.0002	0.186
23	01 31 57.70	-13 36 43.6	22.83 ± 0.03	21.39 ± 0.03	20.68 ± 0.01	17.76 ± 0.03	...	0.180
24	01 31 56.92	-13 36 21.2	19.73 ± 0.01	18.75 ± 0.02	18.16 ± 0.01	15.39 ± 0.01	...	0.281
25	01 31 57.33	-13 36 32.8	22.30 ± 0.02	20.91 ± 0.03	20.13 ± 0.01	17.34 ± 0.03	...	0.160
26	01 31 48.71	-13 36 25.0	21.89 ± 0.02	20.27 ± 0.02	19.46 ± 0.01	16.33 ± 0.01	...	0.186
27	01 31 54.57	-13 36 25.8	23.26 ± 0.04	21.64 ± 0.03	20.46 ± 0.01	16.89 ± 0.02	...	0.425
28	01 31 51.26	-13 36 20.9	22.42 ± 0.02	18.91 ± 0.03	20.24 ± 0.01	17.19 ± 0.03	...	0.175
29	01 31 53.33	-13 36 31.3	20.63 ± 0.01	18.52 ± 0.02	18.46 ± 0.01	15.44 ± 0.01	0.2094 ± 0.0002	0.186
30	01 31 53.84	-13 36 13.0	20.50 ± 0.01	18.90 ± 0.02	18.11 ± 0.01	14.94 ± 0.00	0.2085 ± 0.0002	0.242
31	01 31 49.36	-13 36 06.4	22.05 ± 0.02	20.53 ± 0.02	19.76 ± 0.01	16.78 ± 0.01	0.2133 ± 0.0004	0.165
32	01 31 49.83	-13 36 11.2	21.42 ± 0.01	20.15 ± 0.02	19.41 ± 0.01	16.38 ± 0.01	0.2123 ± 0.0003	0.215
33	01 31 52.97	-13 36 22.3	21.82 ± 0.02	20.16 ± 0.02	19.40 ± 0.01	16.33 ± 0.01	...	0.186
34	01 31 50.86	-13 36 03.8	20.41 ± 0.01	18.78 ± 0.02	18.03 ± 0.01	14.85 ± 0.00	0.2078 ± 0.0002	0.225
35	01 31 50.31	-13 36 01.4	23.47 ± 0.05	21.57 ± 0.03	20.90 ± 0.01	17.84 ± 0.03	...	0.186
36	01 31 53.67	-13 36 03.8	23.18 ± 0.04	21.67 ± 0.03	20.95 ± 0.01	18.19 ± 0.06	...	0.170
37	01 31 50.36	-13 35 52.9	22.43 ± 0.02	20.83 ± 0.02	20.00 ± 0.01	17.01 ± 0.02	...	0.170
38	01 31 56.88	-13 35 51.6	22.66 ± 0.03	21.21 ± 0.03	20.43 ± 0.01	17.53 ± 0.03	...	0.191
39	01 31 30.91	-13 24 42.8	23.19 ± 0.03	...	20.54 ± 0.01	17.29 ± 0.03	...	0.289
40	01 31 22.10	-13 24 37.5	21.17 ± 0.01	...	18.83 ± 0.01	15.77 ± 0.02	...	0.203
41	01 31 33.44	-13 25 02.8	21.78 ± 0.02	...	19.19 ± 0.01	15.68 ± 0.01	...	0.425
42	01 31 25.47	-13 25 15.5	23.26 ± 0.04	...	20.82 ± 0.01	17.75 ± 0.05	...	0.225
43	01 31 28.92	-13 25 19.2	22.63 ± 0.03	...	20.28 ± 0.01	17.25 ± 0.03	...	0.215
44	01 31 26.99	-13 25 07.5	22.57 ± 0.04	...	19.90 ± 0.01	16.86 ± 0.03	...	0.273
45	01 31 26.50	-13 25 13.7	20.85 ± 0.01	...	18.25 ± 0.01	14.91 ± 0.01	...	0.289
46	01 31 20.43	-13 25 20.0	21.95 ± 0.02	...	19.53 ± 0.01	15.92 ± 0.01	...	0.538
47	01 31 33.65	-13 25 32.6	20.61 ± 0.01	...	18.39 ± 0.01	15.37 ± 0.01	...	0.197
48	01 31 30.07	-13 26 04.7	23.01 ± 0.03	...	20.46 ± 0.01	17.20 ± 0.03	...	0.273
49	01 31 17.43	-13 26 04.3	22.60 ± 0.02	...	20.78 ± 0.01	17.56 ± 0.03	...	0.555
50	01 31 25.21	-13 26 33.0	22.90 ± 0.03	...	20.59 ± 0.01	17.57 ± 0.03	...	0.206
51	01 31 24.65	-13 26 08.0	20.21 ± 0.01	...	17.81 ± 0.01	14.77 ± 0.01	...	0.229
52	01 31 34.11	-13 26 35.2	22.65 ± 0.03	...	20.48 ± 0.01	16.61 ± 0.02	...	0.682
53	01 31 29.12	-13 26 38.8	23.32 ± 0.05	...	20.61 ± 0.01	16.68 ± 0.02	...	0.606
54	01 31 33.01	-13 26 46.9	21.74 ± 0.01	...	19.62 ± 0.01	16.73 ± 0.02	...	0.170
55	01 32 00.96	-13 27 06.0	21.03 ± 0.01	...	18.79 ± 0.01	15.79 ± 0.02	...	0.209
56	01 31 45.29	-13 27 14.6	20.83 ± 0.01	...	18.37 ± 0.01	15.24 ± 0.00	...	0.235
57	01 31 48.70	-13 27 28.6	21.40 ± 0.01	...	19.87 ± 0.01	16.93 ± 0.02	...	0.571
58	01 31 51.61	-13 27 34.5	22.55 ± 0.03	...	20.69 ± 0.01	17.37 ± 0.03	...	0.571
59	01 31 22.90	-13 27 32.5	22.76 ± 0.03	...	20.35 ± 0.01	17.18 ± 0.03	...	0.250
60	01 31 40.99	-13 27 22.2	20.97 ± 0.01	...	18.82 ± 0.01	16.05 ± 0.01	...	0.165

heliocentric corrected spectroscopic redshift,  $z_{spec}$  (Col. 8), if available, and the photometric redshift,  $z_{phot}$  (Col. 9).

## 4 GLOBAL CLUSTER PROPERTIES

### 4.1 NIR luminosity function of cluster galaxies

#### 4.1.1 *K*-band Magnitudes and Completeness

To perform source detection, we ran SExtractor (Bertin & Arnouts 1996) on the  $K$ -band mosaic of ABCG 209, obtaining a  $K$ -band catalogue with a total of 2628 objects. For each source, we measured aperture magnitudes within a  $5''$  diameter aperture, and Kron magnitudes within an aperture of diameter  $\alpha \cdot r_K$ , where  $r_K$  is the Kron radius (Kron 1980). We chose  $\alpha = 2.2$ , for which the Kron magnitude is expected to enclose 92% of the total flux, and we computed the total magnitude,  $K$ , by subtracting 0.08 mag from the Kron magnitudes.

As shown in Fig. 3 (left panel), objects were classified as stars and galaxies according to the distribution of sources in the  $SI$  versus Kron magnitude diagram, where  $SI$  is the stellarity index parameter of SExtractor. We classified as stars those objects whose  $SI$  value is larger than a given threshold,  $SI_{min}$ . The value of  $SI_{min}$  was chosen by adding simulated stars and galaxies to the  $K$ -band mosaic, and measuring their  $SI$  and  $m_K$  parameters by means of SExtractor, in the same way as for real sources. Simulated stars and galaxies were randomly generated in a magnitude range of  $K = 14$  mag to  $K = 21$  mag. In order to create the simulated images, we modelled real sources in the  $K$ -band mosaic as the sum of three two-dimensional Moffat functions. The Moffat models were scaled according to the magnitude of simulated objects and added randomly to the  $K$ -band mosaic. In the case of stars, the modelling was performed by fitting non-saturated sources with  $K < 16$  mag and  $SI > 0.9$ . For galaxies, we fitted objects with  $SI < 0.2$ , in a magnitude range of  $K_{min}$  to  $K_{max}$ . We chose  $K_{min} = 17$  mag and  $K_{max} = 18.5$  mag, and we also varied the values of  $K_{min}$  and  $K_{max}$  in order to test the robustness of our completeness estimates (see below) with respect to these parameters. Fig. 3 shows the distribution of simulated objects in the  $SI$  versus  $K$  diagram. At magnitudes brighter than  $K \sim 17.5$  mag, stars and galaxies are clearly well separated, with this separation disappearing at fainter magnitudes. In fact, for  $K \gtrsim 17.5$  mag, simulated stars have a stellarity index  $\gtrsim 0.4$ , while almost all simulated galaxies have  $SI \lesssim 0.8$ . In order to minimise the fraction of misclassified stars and galaxies, we adopted

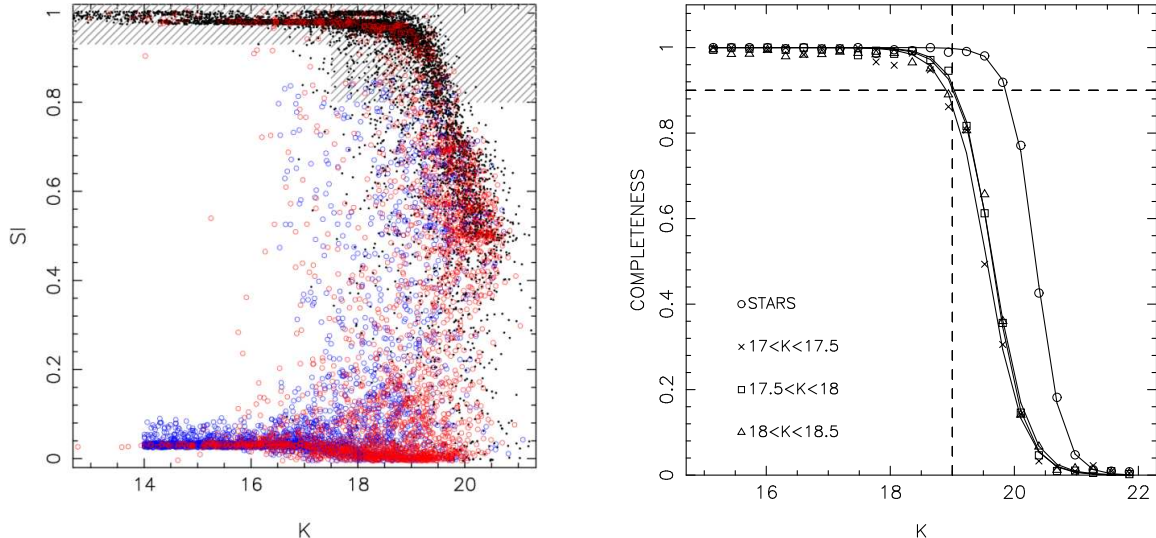


**Figure 3.** *Left panel:* Stellarity index versus  $K$ -band magnitude diagram for all sources detected in the  $K$ -band mosaic of ABCG 209 (red circles), for simulated galaxies (blue circles), and simulated stars (black dots). Shaded area indicates the selection criteria used to identify stars. *Right panel:*  $K$ -band completeness function. Crosses, squares and triangles denote the completeness percentage as estimated by simulating galaxies in different magnitude bins (see the text) as shown in the lower left corner of the panel. The completeness percentage of stars is plotted by the circles. The solid curves represent the fits of the completeness functions by Fermi-Dirac functions. The dashed lines mark a completeness level of 90% for the galaxy catalogue.

a value of  $SI_{\min}$  that depends on the source magnitude, with  $SI_{\min} = 0.95$  for  $K \leq 17.5$  mag and  $SI_{\min} = 0.8$  for  $K > 17.5$  mag. The corresponding star/galaxy classification leads to a sample of 2334 galaxies in the  $K$ -band field of ABCG 209. The completeness of the  $K$ -band catalogue was estimated by measuring the percentage of simulated galaxies and stars which are recovered by SExtractor as a function of  $K$ . The completeness functions are shown in Fig. 3 (right panel) for both stars and galaxies. The figure shows that the  $K$ -band galaxy catalogue of ABCG 209 is complete at more than 90% down to  $K \sim 19$  mag, with the completeness level falling rapidly to  $\sim 50\%$  at  $K \sim 19.5$ , and to  $\sim 20\%$  at  $K \sim 20$  mag. As one would expect, the stellar catalogue is characterised by a higher completeness at a given magnitude, being more than 90% complete down to  $K \sim 19.8$  mag. The figure also shows that the galaxy completeness function does not depend significantly on the magnitude range of the sources used to create simulated galaxies. In fact, changing the values of  $K_{\min}$  and  $K_{\max}$ , as shown in the figure, we found that the completeness estimates do not change significantly.

#### 4.1.2 $K$ -band Luminosity function

The  $K$ -band LF of ABCG 209 was derived in a square region of 4.7 arcmin side size around the cluster center, by computing number counts of galaxies brighter than  $K = 19.5$  mag. Using the simulation results discussed in Sec. 4.1.1, we corrected number counts for (i)

incompleteness, dividing by the completeness function shown in Fig. 3 (right panel), and (ii) contamination from misclassified stars and galaxies, dividing number counts by the expected fraction of misclassified galaxies and subtracting the expected number of misclassified stars in each magnitude bin. Number counts were then corrected for background/foreground galaxies, by using field galaxy counts from the Calar Alto Deep Imaging Survey (CADIS, see Huang et al. 2001), a medium deep  $K$ -band survey with a total area of 0.2 deg $^2$  and a completeness magnitude of 19.75 mag. Since our  $K$ -band photometry is 50% complete down to  $m_K = 19.5$  mag, the CADIS data are a suitable dataset for the estimation of field galaxy counts. The resulting LF of ABCG 209 and its fit with a single Schechter function, are shown in Fig. 4. The error bars on number counts take into account Poissonian uncertainties on both field and cluster counts. The LF fit was performed by a  $\chi^2$  minimisation routine, accounting for the finite size of magnitude bins by integrating the Schechter function in each magnitude bin. Since brightest cluster galaxies usually prevent a good fit of the LF to be achieved with a single Schechter function (see e.g. de Propris et al. 1998 and de Propris et al. 1999), the cD galaxy of ABCG 209 was excluded from the fitting. The Schechter function fit, whose parameters are the faint end slope,  $\alpha$ , and the characteristic magnitude,  $K^*$ , provides a good description of cluster galaxy counts. The only magnitude bin showing a larger deviation is that at  $K = 17.5$  mag, where a marginal ( $\sim 1.5\sigma$  significant) deficiency of cluster galaxies is found. Using an  $R - K$  colour of  $\sim 3.1$ , which is typical of early-type cluster galaxies at  $z \sim 0.2$  (e.g. La Barbera et al. (2004), hereafter LM04), the magnitude of  $K = 17.5$  mag can be transformed to  $R \sim 20.6$  mag, that corresponds to the magnitude bin ( $20 < R < 21$  mag) where Mercurio et al. (2003b) find some indication of a dip in the optical luminosity functions of ABCG 209. The best-fitting value of the  $K$ -band Schechter function parameters turn out to be  $\alpha = -0.98 \pm 0.15$  and  $K^* = 14.80 \pm 0.30$  mag, respectively. The uncertainties on  $\alpha$  and  $K^*$  were derived by randomly shifting galaxy number counts according to their uncertainties, and then re-computing the best-fitting Schechter function. Joint probability contours for  $\alpha$  and  $K^*$  are shown in Fig. 3. The above value of  $\alpha$  is fully consistent with those found from previous studies of NIR luminosity functions of cluster galaxies, such as  $\alpha = \sim 1.0$  (de Propris et al. 1998),  $\alpha \sim -1.3$  (Andreon & Pellò 2000), and  $\alpha \sim -1.2$  (LM04).

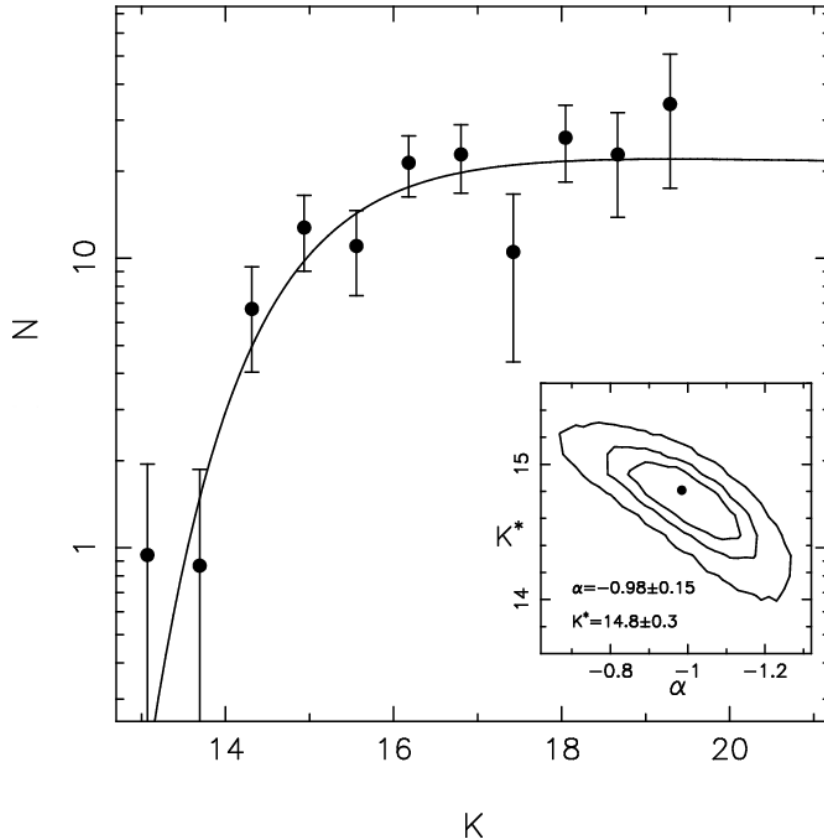


**Figure 4.**  $K$ -band luminosity function of ABCG 209. The solid curve shows the best-fitting Schechter function. The smaller panel in the lower-right corner of the figure shows the joint probability contours of  $K^*$  and  $\alpha$  best-fitting values. Black contours correspond to  $1\sigma$ ,  $2\sigma$ , and  $3\sigma$  standard probability levels, respectively. The best-fitting value of  $K^*$  and  $\alpha$  are also reported in the lower-left corner of the smaller panel.

## 4.2 Dynamical properties

In a previous paper we investigated the dynamical status of the galaxy cluster ABCG 209, analysing a sample of 119 spectra with  $8 \text{ \AA}$  resolution and selecting 112 galaxies belonging to the cluster (Mercurio et al. 2003a). Hereafter we will refer to this sample as the “old sample”. Among the old sample, 22 galaxies were observed again at higher resolution within the two masks together with 29 new galaxies. Combining the old and new redshifts we obtained a total sample of 148 galaxies. In Table 1 we report spectroscopic redshift measurements of the new observed galaxies.

### 4.2.1 Member selection

In order to select cluster members, we analysed the velocity distribution by applying the one-dimensional adaptive kernel technique (Pisani 1993, as implemented by Fadda et al. 1996 and Girardi et al. 1996). This procedure confirms the existence of a single peak at  $z \sim 0.209$ , consisting of 134 cluster members. Moreover, this procedure indicates two other

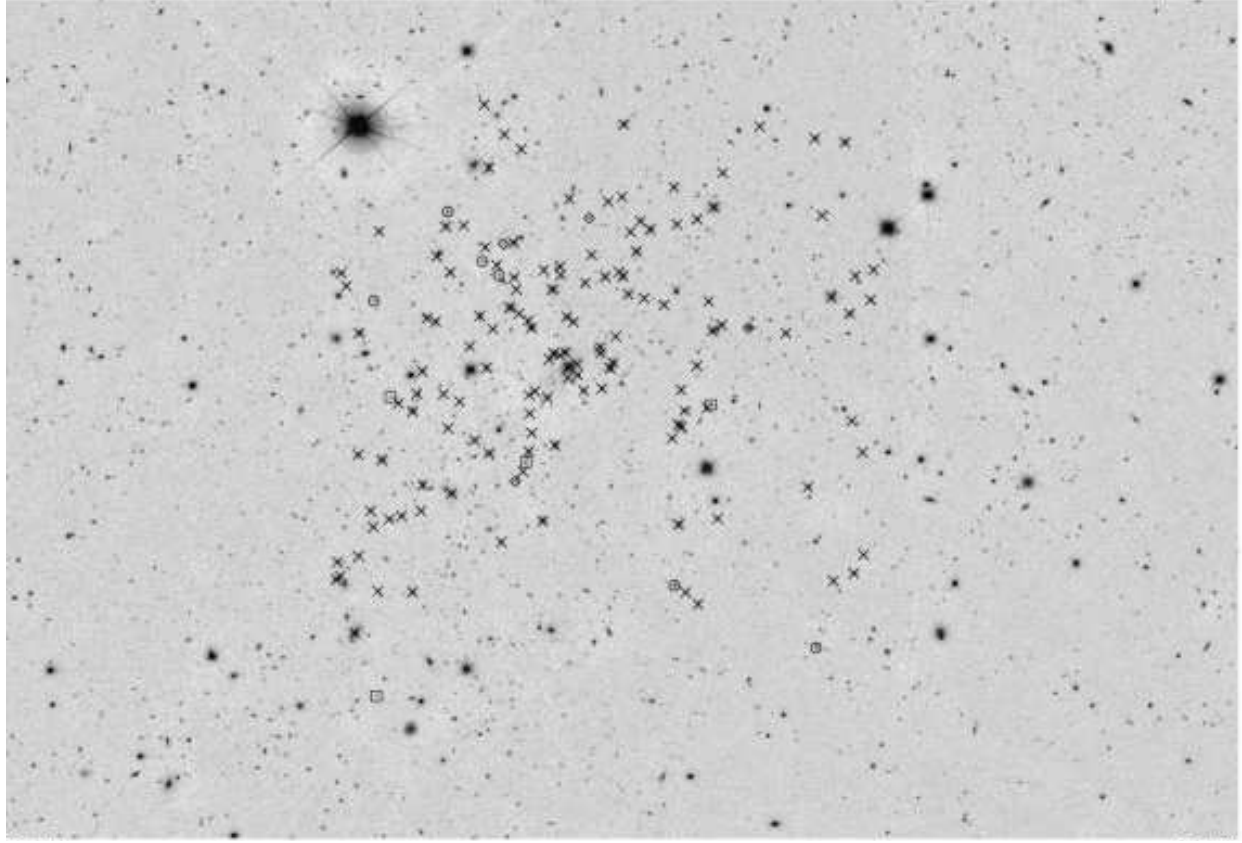


**Figure 5.** CFHT R-band image of ABCG 209 (North at top and East to left). Galaxies belonging to the cluster are marked with crosses, galaxies at  $z \sim 0.257$  with circles, galaxies at  $z \sim 0.392$  with squares and the remaining isolated galaxies with diamonds.

possible structures at higher redshifts, one at  $z \sim 0.257$  with 6 candidate members, and another at  $z \sim 0.392$  with 4 candidate members. The remaining 4 galaxies are considered field galaxies. Although the structure at  $z \sim 0.257$  has a high significance (96.6%), the low number of galaxies prevents us from assessing the existence of a background cluster. In Fig. 5 we show the 134 cluster members as crosses, the 6 galaxies at  $z \sim 0.257$  as circles and the 4 galaxies at  $z \sim 0.392$  as squares. Figure 6 shows the redshift distribution of the 148 observed galaxies. The mean redshift of the cluster as derived by the biweight estimator (Beers et al. 1990) is  $\langle z \rangle = 0.2090 \pm 0.0004$ .

We further explored the possibility of contamination by interlopers by applying the “shifting gapper” algorithm of Fadda et al. (1996). This procedure rejects galaxies that are too far in velocity-space from the main body of cluster galaxies within a fixed radial bin, shifting along the distance from the cluster centre. Following the prescriptions of Fadda et al. (1996) we used a gap of  $1000 \text{ km s}^{-1}$  and a bin of  $0.6 h_{70}^{-1} \text{ Mpc}$ , or large enough to include at least 15 galaxies. In this case eight galaxies were rejected (cf. crosses in Fig. 7).

In order to determine the cluster centre, we applied the two-dimensional adaptive kernel

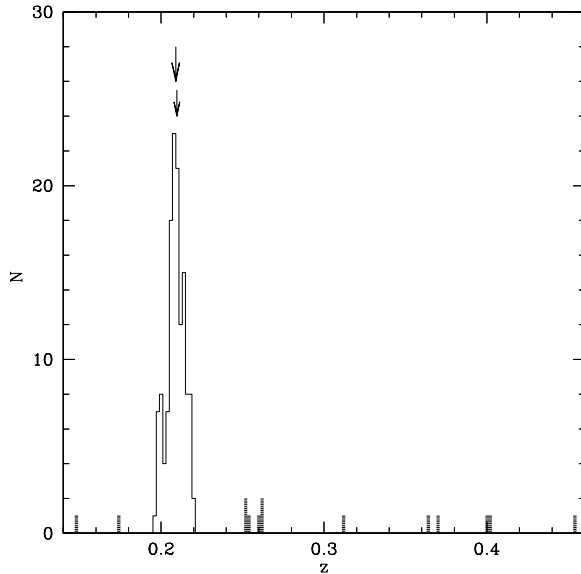


**Figure 6.** Distribution of redshifts for the 148 observed galaxies. The big and small arrows indicate the mean cluster redshift and the redshift of the cD galaxy, respectively. Black areas mark galaxies not belonging to the cluster.

technique to the galaxy positions. The centre of the most significant peak ( $\alpha = 01^{\circ}31'52.59$ ,  $\delta = -13^{\circ}36'45.9$ ) is coincident with the position of the cD galaxy and only  $4''$  distant from that of the old sample.

#### 4.2.2 Velocity dispersion

We estimated the line-of-sight velocity dispersion (LOSVD),  $\sigma_v$ , using the biweight estimator (ROSTAT package; Beers et al. 1990). After applying the relativistic correction and the usual correction for velocity errors (Danese et al. 1980), considering only the 126 galaxies selected by the "shifting gapper" method, we obtained  $\sigma_v = 1268^{+93}_{-84}$  km s $^{-1}$ , where errors were estimated with the bootstrap method. If we consider all the 134 galaxies we obtain  $\sigma_v = 1390^{+91}_{-91}$  km s $^{-1}$ . This value is slightly larger, but fully consistent with the value computed excluding the galaxies identified as outliers by the "shifting gapper" method.

Velocity anisotropies in the galaxy distribution can create problems in determining the LOSVD. For this reason we plot in Fig. 8 the cluster velocity (upper panel) and the velocity dispersion (lower panel) vs. projected clustercentric distance. This shows that the  $\sigma_v$ , computed by including larger and larger regions, decreases in the central cluster regions, but flattens out in the external regions, suggesting that the value of the LOSVD is no longer affected by velocity anisotropies. The rejection of the eight galaxies due to the application of the shifting gapper (cf. crosses in Fig. 7) leads only to a small variation in the estimate

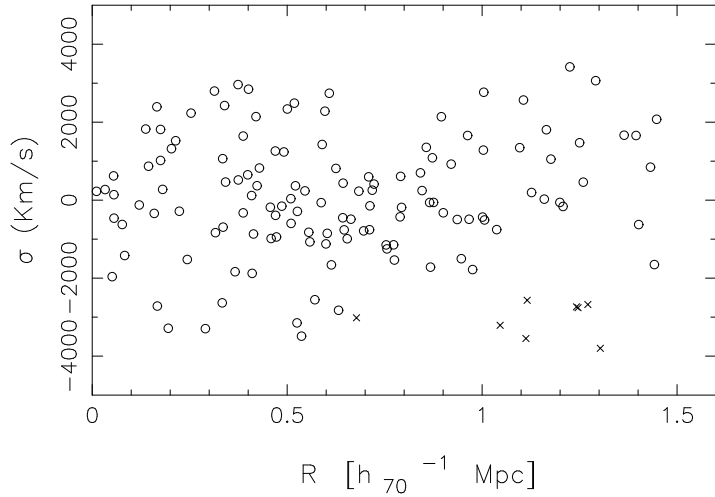


**Figure 7.** Velocity in the cluster rest frame vs. (projected) clustercentric distance for the 134 selected members. The application of the “shifting gapper” method with a bin of  $0.6 \text{ } h_{70}^{-1} \text{ Mpc}$  rejects the eight galaxies indicated by crosses.

of  $\sigma_v$  and in the velocity dispersion profile (see dot-dashed line in Fig. 8) so we confirm our first result of Mercurio et al. (2003a) that the high value of velocity dispersion is connected to the strong dynamical evolution of the cluster. In fact, this large value is already reached at a radius of  $0.4\text{--}0.5 \text{ } h_{70}^{-1} \text{ Mpc}$ , where the contamination of interlopers is expected to be negligible.

#### 4.2.3 Velocity dispersion of red sequence galaxies

In order to further investigate the possible enhancement of the velocity dispersion due to projection effects from infalling galaxies in the centre of the cluster we obtain the velocity dispersion profile considering only galaxies lying on the Colour-Magnitude relation (CMR).

We obtained the CMR by fitting the photometric data of the spectroscopically confirmed cluster members and those galaxies with photometric redshift in the range  $0.14 - 0.26$  (see Sect. 3.2) with a biweight algorithm (Beers et al. 1990), obtaining:

$$(R - K)_{\text{CM}} = 4.673 - 0.096 \cdot R . \quad (1)$$

By using Eq. 1, we defined as sequence galaxies the sources lying in the region inside the curves:

$$(R - K)_{\text{seq}} = (R - K)_{\text{CM}} \pm 2 \cdot \left( \sqrt{\sigma_R^2 + \sigma_K^2} + 0.05 \right) ,$$

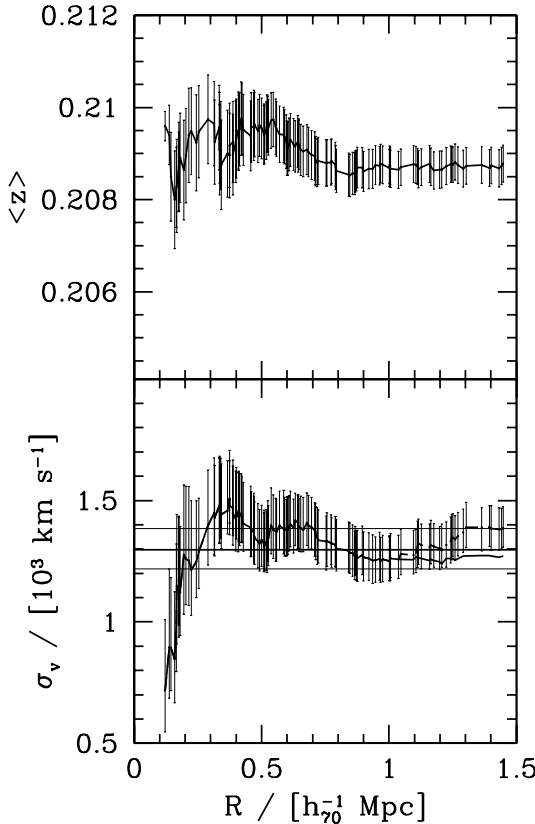


**Figure 8.** Integrated mean redshift and LOSVD profiles for the 134 galaxies (upper and lower panel, respectively) at a given projected distance from the cluster centre, estimated by considering all the galaxies within this radius. The error bars at the 68% c.l. are shown. In the lower panel, solid and dot-dashed lines give the profile after and before the rejection of eight possible interlopers according to the “shifting gapper” method, respectively. The horizontal lines represent X-ray temperature with the respective errors transformed in  $\sigma_v$  imposing  $\beta_{spec} = 1$ , where  $\beta_{spec} = \sigma_v^2 / (kT / \mu m_p)$ , with  $\mu$  the mean molecular weight and  $m_p$  the proton mass.

where we take into account the uncertainty at  $2\sigma$  both on the  $R$  ( $\sigma_R$ ) and on the  $K$  magnitude ( $\sigma_K$ ) as well as the intrinsic dispersion of the CMR (e.g., Merluzzi et al. 2002, 2003).

We select 96 spectroscopically confirmed member galaxies lying on the CMR (filled circles in Fig. 9), obtaining a LOSVD for the red sequence galaxies of  $\sigma_{v,CMR} = 1232^{+94}_{-92} \text{ km s}^{-1}$ . By selecting galaxies on the CMR, we expect to include only early-type galaxies and to minimise the effect of infalling late type galaxies on the line-of-sight velocity dispersion. However the measured value of the LOSVD and the velocity profile shown in Fig. 10 are fully consistent with those obtained considering all the sample (see dashed line in Fig. 10).

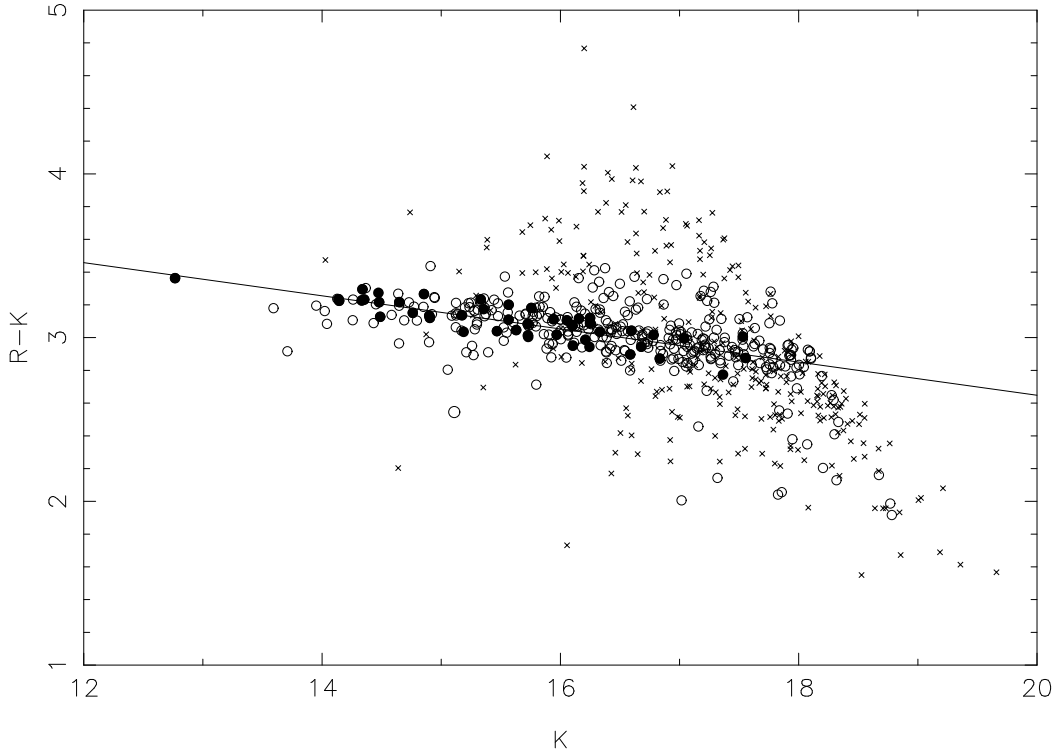


**Figure 9.** The R-K/R colour-magnitude diagram of the cluster galaxy population. Open circles indicate galaxies with photometric redshift in the range 0.15-0.30 and crosses represent the other galaxies with photometric data. The solid line indicates the best-fitting C-M relation of Eq. 1, and spectroscopically confirmed member galaxies identified as belonging to the red sequence through Eq. 4.2.3 are indicated by solid circles.

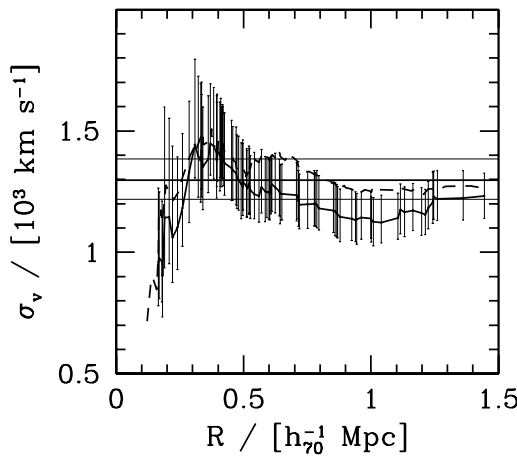


**Figure 10.** Integrated LOS velocity dispersion profile for the 96 galaxies at a given projected distance from the cluster centre, estimated by considering all the galaxies within this radius. The error bars at the 68% c.l. are shown. Solid and dashed lines give the profile considering only red sequence galaxies and all the cluster member galaxies after the rejection of eight possible interlopers according to the “shifting gapper” method, respectively. The horizontal lines represent X-ray temperature with the respective errors transformed in  $\sigma_v$  imposing  $\beta_{spec} = 1$ , where  $\beta_{spec} = \sigma_v^2 / (kT / \mu m_p)$ , with  $\mu$  the mean molecular weight and  $m_p$  the proton mass.

#### 4.2.4 Virial radius and mass

Assuming that galaxies are in dynamical equilibrium with the cluster potential we can determine the cluster mass from the knowledge of positions and velocities of the member galaxies by applying the virial theorem. Since the application of the virial theorem is meaningful only when the system is in dynamical equilibrium within the considered region, a natural choice is to compute the cluster mass,  $M_{\text{vir}}$ , inside the radius of virialization,  $R_{\text{vir}}$ , within which the cluster can be considered to be not far from dynamical equilibrium.

Following the prescriptions of Eq. 1 of Girardi & Mezzetti (2001):  $R_{\text{vir}} = 0.17 \times \sigma_v / H(z)$ , where  $H(z) = H_0(1+z)^{3/2}$  (see also Eq. 8 of Carlberg et al. 1997 for  $R_{200}$ ) and  $\sigma_v$  is a “robust” estimate of the line-of-sight velocity dispersion. We indicate as robust a value that is not affected by the presence of velocity anisotropies in the galaxy orbits that can strongly influence the central cluster regions. Following Fadda et al. 1996), we check the robustness of  $\sigma_v$  from the analysis of velocity dispersion profile. Since the profile flattens out in the external regions (see Fig. 8), our estimate of the velocity dispersion is robust (see Sect. 4.2.2).

In a  $\Lambda$ CDM model, with  $\Omega_M = 0.3$ ,  $\Omega_\Lambda = 0.7$  and  $H_0 = 70 \text{ km s}^{-1}$ , the value of  $\sigma_v = 1268^{+93}_{-84} \text{ km s}^{-1}$  leads to a value of the virial radius  $R_{\text{vir}} \sim 3.42 h_{70}^{-1} \text{ Mpc}$ . In our previous work (Mercurio et al. 2003a), we considered a flat universe with  $\Omega_M = 1$ . In this case the collapsed region for a spherical model corresponds to the region inside  $R_{178}$ . For a comparison with our previous estimates we derive  $R_{178} \sim 2.31 h_{70}^{-1} \text{ Mpc}$ .

On the hypothesis that the galaxy distribution traces the mass distribution we obtain from the virial theorem (Limber & Mathews 1960):

$$M_{\text{vir}} = \frac{2 \langle v^2 \rangle}{G \langle r_{ij}^{-1} \rangle} = \frac{\sigma^2 R_{\text{vir}}}{G}, \quad (2)$$

where  $v$  is the galaxy velocity referred to the cluster mean velocity,  $r_{ij}$  is the distance between any pair of galaxies,  $\sigma$  is the global velocity dispersion.

Assuming that the cluster is spherical, non-rotating system, we can use the projected velocity dispersion  $\sigma_v$  and the projected virial radius,  $R_{PV}$ . Therefore, Eq. 2 becomes:

$$M_{\text{vir}} = \frac{3\pi}{2} \frac{\sigma_P^2 R_{PV}}{G}. \quad (3)$$

In this formula  $R_{PV}$  is the projected radius, equal to twice the (projected) harmonic radius:

$$R_{PV} = \frac{N(N-1)}{\sum_{i>j} R_{ij}^{-1}}, \quad (4)$$

where  $R_{ij}^{-1}$  is the projected distance between two galaxies and  $N$  is the number of observed

galaxies. The value of  $R_{PV}$  depends on size of the sampled region, and on the quality of the sampling. In particular, it increases with the cluster aperture  $A$  within which it is estimated.

In our data the cluster is sampled out to a radius of  $R \sim 1.5h_{70}^{-1}$  Mpc or  $\sim 0.6R_{178}$ , but we uniformly sample the region  $R_{max} \sim 1.0h_{70}^{-1}$  Mpc or  $\sim 0.4R_{178}$ . If we consider only the region of the cluster that is well sampled, we obtain  $R_{PV} = (0.73 \pm 0.05)h_{70}^{-1}$  Mpc (the error is obtained through the jackknife method) within  $A = R_{max}$ . Although the cluster is not sampled out to  $R_{178}$ , we can estimate  $R_{PV}$  at  $A = R_{178}$  theoretically from the knowledge of the parameters  $\alpha$  and  $R_C$  of the King-like distribution. We can use Eq. 13 of Girardi et al. (1998). In this case  $R_{PV} = 1.48h_{70}^{-1}$  Mpc.

When the system is not entirely included in the observational sample, the usual form of the virial theorem  $2T + V = 0$  should be replaced by  $2T + V = 3PV$ , where  $3PV$  is the surface pressure term (e.g., The & White 1986). Therefore, a surface pressure term  $C$  should be applied to the mass estimate:

$$M_c = M_{vir} - C \quad . \quad (5)$$

The value of the surface pressure term correction  $C$  can be obtained by analysing the velocity dispersion profile, but this procedure requires several hundreds of member galaxies. Combining data of many clusters, Girardi & Mezzetti (2001) obtained that velocities are isotropic and that the correction at  $R \sim R_{vir}$  is  $C = 0.2M_V$  (e.g. Carlberg et al. 1997, Girardi et al. 1998). Then, following this approach we can estimate the mass of the system inside the collapsed region, assuming a value of 20% for the surface pressure term correction. This leads to a value of total mass  $M_c(< R_{178}) = 2.12_{-0.48}^{+0.47} \times 10^{15} h_{70}^{-1} M_\odot$ , while in a  $\Lambda$ CDM model, with the adopted cosmology  $M_c(< R_{vir}) = 2.95_{-0.78}^{+0.80} \times 10^{15} h_{70}^{-1} M_\odot$ .

## 5 DYNAMICAL ANALYSIS

### 5.1 Velocity distribution

In order to perform a robust description of the velocity distribution and to detect possible subclumps we applied the 1D KMM algorithm (Ashman et al. 1994) to the 126 galaxy sample, selected by the “shifting gapper” method, and to the original sample of the 134 galaxies. The KMM algorithm fits a user-specified number of Gaussian distributions to a dataset and assesses the improvement of that fit over a single Gaussian. In addition, it provides the maximum-likelihood estimate of the unknown n-mode Gaussians and an

assignment of objects into groups. The KMM algorithm is most appropriate in situations where theoretical and/or empirical arguments indicate that a Gaussian model is valid, as in the case of the cluster velocity distributions, where gravitational interactions drive the system toward a relaxed configuration with a Gaussian velocity distribution, but one of the major uncertainties of this method is the optimal choice of the number of groups for the partition.

For this reason, we first investigate the presence of gaps in the velocity distribution using the ROSTAT package (Beers et al. 1990), which has the advantage of not requiring any *a priori* assumption for the shape of the distribution. Within this package, a gap is defined as the difference between two contiguous velocities, weighted by the distances of these velocities with respect to their average. We considered only normalised gaps larger than 2.54 since, by considering a random sampling of a Gaussian distribution, such gaps appear only in less than 1.4% of the cases, independently of the sample size. We found four significant gaps indicated by continuous (3.88, 0.05% of the cases), dotted (3.25, 0.10% of the cases), dashed (2.59, 1.4% of the cases) and dot-dashed (2.57, 1.4% of the cases) arrows in the lower panel of Fig. 11. We underline that those gaps are found by using all the 134 galaxies in the sample, but identical results are obtained considering only 126 galaxies.

Using the results of the weighted-gap analysis we divide galaxies into five groups and we apply the 1D KMM. From the maximum likelihood statistics, however, we found that a mixture of five Gaussians do not give a good description of the data (45.7% c.l.). Then we divide galaxies in four groups and we apply the 1D KMM, but from the maximum likelihood statistics, we found that the data can be described as a mixture of four Gaussians at only 89.7% c.l. On the other hand, from the maximum likelihood statistics we found that a mixture of three Gaussians is the best description of the velocity distribution (at 98.4% c.l.). In the upper panel of Fig. 11 we plot the velocity distribution of galaxies with, superimposed, the three Gaussians corresponding to the three identified clumps. The most prominent gap detected by the ROSTAT package is between the clumps 1 and 2 identified by the KMM algorithm. Using the one dimensional KMM algorithm we assigned the member galaxies to individual groups ( $n_1=16$ ,  $n_2=102$ , and  $n_3=16$  members at mean redshift  $z_1 = 0.1988$ ,  $z_2 = 0.2090$ , and  $z_3 = 0.2172$ ) and we estimate the velocity dispersion of  $\sigma_{v1} = 323^{+47}_{-58}$  km s $^{-1}$ ,  $\sigma_{v2} = 847^{+52}_{-49}$  km s $^{-1}$ , and  $\sigma_{v3} = 289^{+57}_{-54}$  km s $^{-1}$  (see Fig. 11) for each clump. We note that the old sample of 112 member galaxies did not allow us to associate galaxies to the less populated substructures and then to obtain a reliable estimation of their velocity dispersions.

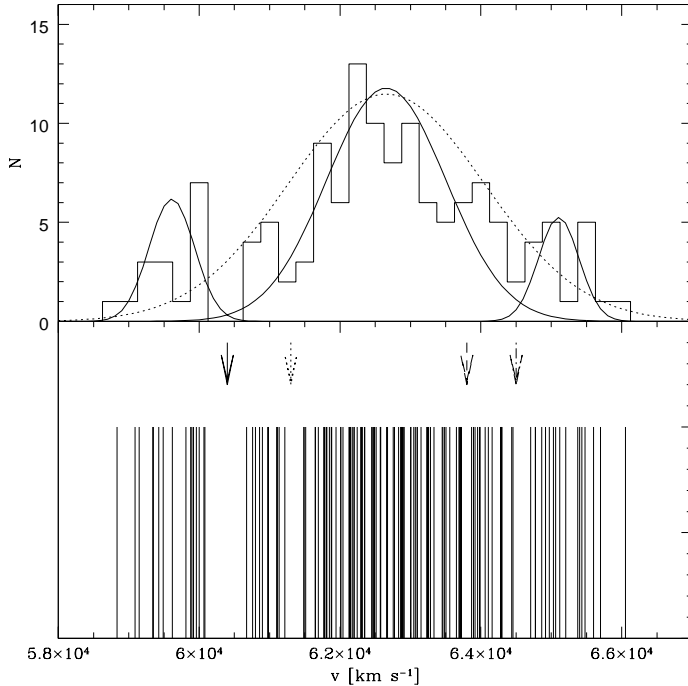


**Figure 11.** Distribution of radial velocities for member galaxies. *Upper panel:* velocity histogram with a bin of  $250 \text{ km s}^{-1}$ , with the three solid Gaussians showing the best separation into three clumps as identified with the one-dimensional KMM test (see text), and the dotted Gaussian indicating the best-fit single Gaussian function to the velocity distribution. *Lower panel:* stripe density plot. The arrows indicate the positions of the three significant gaps in the velocity distribution of member galaxies (see Beers et al. 1991).

Figure 12 shows the spatial distributions of the three clumps. Differently from the results of our first paper, we find no evidence for spatial segregation for the three clumps, according to the two-dimensional Kolmogorov-Smirnov test (hereafter 2DKS-test; cf. Fasano & Franceschini 1987, as implemented by Press et al. 1992).

## 5.2 3D substructures

In order to check for the presence of substructure, we combined velocity and position information by computing the  $\Delta$ -statistic devised by Dressler & Schectman (1988). This test is sensitive to spatially compact subsystems having an average velocity and/or a velocity dispersion different from the global mean quantities. We found a value of 198 for the  $\Delta$  parameter, which gives the cumulative deviation of the local kinematical parameters (velocity mean and velocity dispersion) from the global cluster parameters. The significance of substructure was checked by running 1000 Monte Carlo simulations, randomly shuffling the galaxy velocities, obtaining a significance level of 99.8%. This indicates that the cluster has a complex structure. In Fig. 13 we plot the member galaxies marked by circles whose

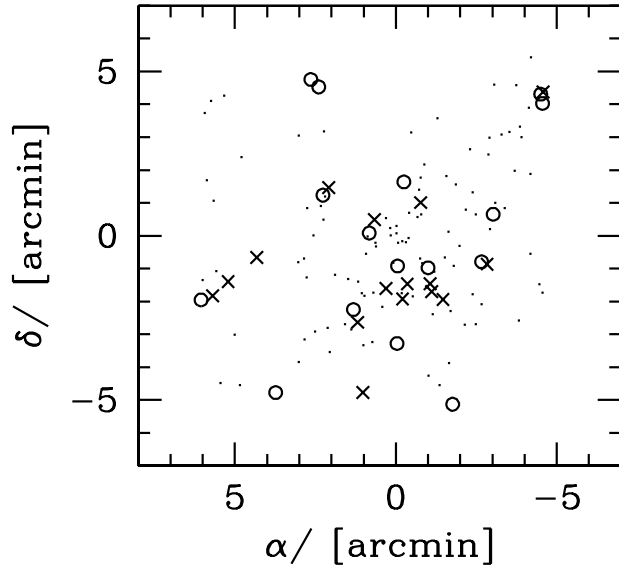


**Figure 12.** Distribution of member galaxies separated into three clumps according the one-dimensional KMM test. The plot is centred on the cluster centre. Open circles, dots and crosses indicate clumps 1, 2 and 3, having low, intermediate and high velocities, respectively.

diameter is proportional to the deviation  $\delta$  of the individual parameters (position and velocity) from the mean cluster parameters. We confirm with this larger sample the results of the previous paper. In particular, a group of galaxies with high velocity in the external East cluster region and another group near the cluster centre could cause the large values of  $\delta$ . We also underline that we obtain a value of 199 for the  $\Delta$  parameter with a significance level of 99.9%, by considering only the 126 galaxies selected with the shifting gapper method.

Since the technique by Dressler & Schectman does not allow a direct identification of galaxies belonging to the detected substructure, we apply the three dimensional version of the KMM test using simultaneously galaxy positions and velocities. We use the galaxy separation obtained in the 1D analysis as first guess of the 3D analysis. The algorithm fits a three-group partition at 98.6% c.l., with a galaxy distribution similar to those obtained by the 1D analysis ( $n_1=16$ ,  $n_2=108$ , and  $n_3=10$  members). On the other hand the 3D KMM fits a four-group partition at 100.0% c.l., with a partition similar to those obtained in the gap analysis performed with the ROSTAT package ( $n_1=16$ ,  $n_2=32$ ,  $n_3=29$ , and  $n_4=47$  members). However, this test seems to be too sensitive to changes in the initial conditions, in fact with a particular choice of the initial group partition it is possible to obtain a separation into two groups significant at 98.0% c.l.

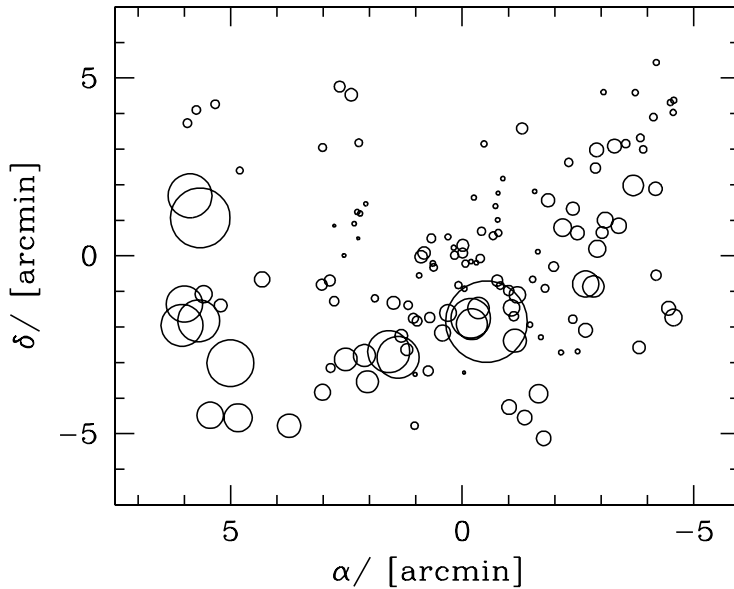


**Figure 13.** Spatial distribution on the sky of the 134 cluster members, each marked by a circle: the larger the circle, the larger is the deviation  $\delta$  of the local parameters from the global cluster parameters. The figure shows evidence for substructure according to the Dressler & Schectman test. The plot is centred on the cluster centre.

## 6 STRUCTURAL PROPERTIES OF EARLY-TYPE GALAXIES

### 6.1 Structural parameters

We derived the structural parameters, namely half-light radius,  $r_e$ , average surface brightness inside  $r_e$ ,  $\mu_e$ , and Sersic shape parameter,  $n$ , in the R and K band for a large sample of galaxies belonging to ABCG 209.

Structural parameters were derived for galaxies in the R-, and K-band, by using the 2DPHOT package (La Barbera et al. 2008).

We considered the sample of spectroscopically confirmed cluster members, complemented with the galaxies having photometric redshift in the range of  $0.14 - 0.26$  (see Sect. 3.2). We found that for Structural parameters were derived for galaxies with  $R < 21.0$  mag and  $K < 17.5$ , i.e. the limits of spectroscopic observations, leading to a total sample of 327 galaxies. Numerical simulation were performed in order to check the reliability of the derived structural parameters, finding that the typical errors were  $\delta(\log r_e) \sim 0.14$  and  $\delta(<\mu_e>) \sim 0.55$  on the effective radius and surface brightness respectively.

Structural parameters were derived by fitting galaxy images with seeing-convolved Sersic models. The point-spread functions (PSFs) were derived locally from the stars in the R and K images and were modelled by a sum of 2D Moffat functions, also taking into account deviations of stellar isophotes from circular symmetry.

Details on the different aspects of the derivation of structural parameters may be found in La Barbera et al. (2002), (2003a), (2003b) and (2008).

The structural parameters are given in Table 3 for the whole sample of 327 galaxies with photometric and spectroscopic redshifts. We remark that this constitutes so far the largest sample of (optical plus NIR) structural parameters of galaxies belonging to one cluster.

## 6.2 Kromendy relation and Photometric Plane

ETGs define a remarkable correlation between the effective radius  $r_e$  and the mean surface brightness  $\langle \mu_e \rangle$ , known as Kormendy relation (KR, Kormendy 1977):

$$\langle \mu_e \rangle = \alpha + \beta \log r_e .$$

In order to study the Kormendy relation (hereafter KR), we selected the population of spheroids on the basis of the shape of the light profile, as parameterised by the Sersic index  $n$ . We classified as spheroids the galaxies with  $n > 2$ , corresponding to objects within a bulge fraction greater than  $\sim 20\%$  (see Saglia et al. 1997; van Dokkum et al. 1998). Moreover, 17 and 54 objects in R and K-band respectively, with small radii were excluded by selecting only galaxies with  $r_e$  greater than 1 pixel.

Again, we point out that the present samples constitute the largest data set of galaxies belonging to one cluster for which the KR is obtained. In fact 240 and 227 galaxies are identified as spheroids in R and K band respectively, with spectroscopic redshift or photometric redshift in the range 0.14 – 0.26 (see above).

Since selection effects can strongly affect the estimate of the KR coefficients (see Ziegler et al. 1999), we fitted the  $\log r_e - \langle \mu_e \rangle$  sequences by introducing a modified least-squares (MLS) procedure (see La Barbera et al. 2003b), which corrects the bias due to the different completeness cuts in magnitude of each sample. The fitting coefficients were derived by applying the bisector regression (see Akritas & Bershady 1996).

Figure 14 shows the KR for R (left panel) and K band (right panel), reporting also the correlation between  $\delta \log r_e$  and  $\delta \langle \mu_e \rangle$ , with the typical values of the uncertainties on the effective parameters. We obtain zero points  $\alpha = 19.19 \pm 0.07$  and  $\alpha = 15.68 \pm 0.07$ , and slopes  $\beta = 3.07 \pm 0.16$  and  $\beta = 3.26 \pm 0.19$  for R and K bands, respectively.

The difference in the zero points is fully consistent with the colour R-K of galaxies, according to the CM relation (Fig. 9).

The slope of the KR in R band is fully consistent with that derived in La Barbera et al.

**Table 3.** Structural parameters of galaxies in ABCG 209, according to the photometric redshifts. Right ascension and declination (Col. 1, Col. 2) effective radius, mean surface brightness and Sersic index for R (Col. 3, Col. 4, Col. 5) and K band (Col. 6, Col. 7, Col. 98)

$\alpha$	$\delta$	$<\mu_R>_e$	$r_{e,R}$	$n_R$	$<\mu_K>_e$	$r_{e,K}$	$n_K$
01 31 47.233	-13 35 31.20	20.6688	0.5633	4.2156	17.1582	0.4069	2.1719
01 31 49.460	-13 37 26.92	19.8916	1.1842	1.9660	17.5605	1.5770	6.7775
01 31 55.678	-13 37 19.92	20.6329	0.3558	3.6644	15.7226	0.2460	1.6739
01 31 51.557	-13 37 18.00	...	...	...	...	...	...
01 31 51.277	-13 37 17.55	...	...	...	...	...	...
01 31 56.403	-13 37 18.23	...	...	...	15.7226	0.2460	1.6739
01 31 54.593	-13 37 04.27	19.4932	0.2552	3.4488	...	...	...
01 31 55.124	-13 37 04.70	20.6571	1.0807	4.3701	16.4715	0.6599	4.1874
01 31 55.177	-13 36 57.94	22.3937	3.2107	7.4987	17.3259	1.1985	7.6776
01 31 51.069	-13 36 27.59	20.2655	0.2876	1.7283	17.4428	0.4174	1.2552
01 31 52.292	-13 36 58.27	20.5305	1.8861	4.4878	16.8956	1.5686	5.3478
01 31 51.793	-13 36 54.83	19.6565	0.3473	4.8037	...	...	...
01 31 52.522	-13 36 27.50	20.5520	0.6928	2.0695	16.9357	0.5250	2.6691
01 31 53.251	-13 36 44.19	19.1673	0.2396	7.7844	...	...	...
01 31 52.868	-13 36 35.24	...	...	...	18.2153	0.8581	9.9032
01 31 52.570	-13 36 44.18	...	...	...	16.7582	0.6264	5.8563
01 31 52.526	-13 36 40.46	22.0511	6.7923	2.9558	20.3538	21.9563	5.2298
01 31 50.965	-13 36 49.60	22.0171	1.9828	7.1752	16.8061	0.5905	3.6298
01 31 56.222	-13 36 46.75	21.9203	2.6347	3.7004	17.7281	1.2374	2.1518
01 31 48.638	-13 36 46.60	19.7038	0.2758	4.3260	17.2784	0.3859	3.8515
01 31 51.318	-13 36 56.77	21.9856	4.3616	9.6712	16.9624	1.5630	4.9491
01 31 57.703	-13 36 43.59	19.8645	0.2750	2.4002	16.8334	0.2815	1.5780
01 31 57.325	-13 36 32.77	20.6240	0.5081	1.4938	17.9624	0.5168	0.8189
01 31 48.709	-13 36 25.01	19.7810	0.4451	1.4137	16.1749	0.3776	2.2878
01 31 51.259	-13 36 20.88	20.1945	0.3756	1.8985	17.4433	0.4172	1.2512
01 31 53.329	-13 36 31.32	19.2165	0.5749	6.5730	16.0117	0.5300	4.4363
01 31 53.837	-13 36 13.04	19.4277	0.7632	3.8471	15.6959	0.6156	4.1877
01 31 49.361	-13 36 06.45	19.4235	0.3293	1.9263	16.4016	0.3427	1.5411
01 31 49.825	-13 36 11.24	19.6579	0.4963	6.3710	16.3664	0.4081	2.4116
01 31 52.968	-13 36 22.32	19.0905	0.3023	1.9196	15.7089	0.3013	5.0108
01 31 50.863	-13 36 03.80	20.0735	1.0809	3.7781	16.5416	0.9476	3.5447
01 31 50.312	-13 36 01.40	...	...	...	...	...	...
01 31 53.668	-13 36 03.78	21.0414	0.4024	1.5757	...	...	...
01 31 50.356	-13 35 52.89	19.0362	0.2349	0.3000	16.4482	0.2815	0.3000
01 31 56.881	-13 35 51.56	20.5237	0.4220	2.0263	17.8736	0.4903	1.0736
01 31 22.104	-13 24 37.48	19.6973	0.5614	2.3988	...	...	...
01 31 25.470	-13 25 15.52	21.4579	0.5904	4.6591	17.0320	0.3165	6.0199
01 31 28.920	-13 25 19.18	19.6969	0.2542	0.7850	16.8525	0.3937	5.8122
01 31 33.649	-13 25 32.56	20.5194	1.1055	2.9986	17.3696	1.1272	3.3754
01 31 25.207	-13 26 33.00	...	...	...	...	...	...
01 31 24.652	-13 26 08.03	21.0140	2.0250	6.1824	17.2039	1.5147	8.1053
01 31 33.012	-13 26 46.86	20.7910	0.7239	3.0107	17.6311	0.6161	1.7465
01 32 00.956	-13 27 05.96	18.5969	0.3669	3.8551	16.0508	0.4125	1.2808
01 31 45.290	-13 27 14.58	19.2001	0.6152	4.1630	15.3983	0.5332	6.6005
01 31 22.896	-13 27 32.46	19.7890	0.2410	2.9062	16.7471	0.3168	2.9581
01 31 40.989	-13 27 22.20	21.4567	1.4440	2.9251	17.9830	1.0992	3.1077
01 31 32.956	-13 27 25.09	20.3794	0.6837	2.7252	17.2724	0.6821	4.1649
01 31 30.360	-13 27 08.93	21.5145	2.1049	3.1130	19.5043	4.4167	6.1853
01 31 57.443	-13 28 15.91	20.2850	0.3420	3.9310	16.9001	0.2943	1.8631
01 31 35.616	-13 28 16.12	22.6539	2.3584	6.4603	20.3706	3.8516	8.9163
01 31 21.567	-13 28 27.36	...	...	...	...	...	...
01 31 19.450	-13 28 16.76	18.3187	0.2393	5.4436	...	...	...
01 31 46.413	-13 28 29.23	21.6343	1.2590	2.7800	19.2229	1.9042	4.0375
01 31 27.472	-13 28 36.00	18.6471	0.3872	3.1090	...	...	...
01 31 19.532	-13 28 46.75	20.5445	0.3773	3.9486	16.6523	0.2603	4.8619
01 31 34.200	-13 28 51.22	19.7480	0.5969	3.1140	16.6719	0.5749	3.4278
01 31 21.362	-13 28 48.04	20.2568	0.4839	2.3031	16.5964	0.3630	2.8755
01 31 28.102	-13 28 54.14	18.5654	0.2678	4.6348	16.3346	0.4461	7.1639
01 31 28.097	-13 28 57.45	21.1347	1.3199	6.0171	17.0114	0.8716	8.5200

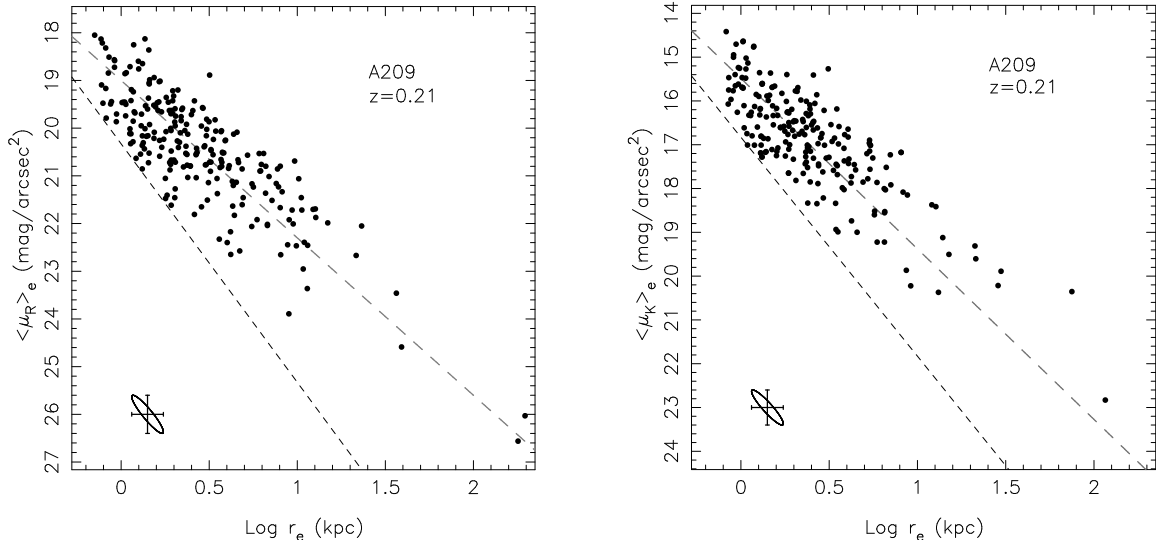


**Figure 14.** Kormendy relations for ABCG 209 in R (right panel) and K band. MLS<sub>logr<sub>e</sub></sub> is represented by long dashed lines. The short dashed line indicate the cuts in total magnitude. The correlation of the uncertainties on logr<sub>e</sub> and <μ<sub>e</sub>> is shown by the ellipses (1 σ confidence contours) in the lower left of each panel.

(2003b) for a smaller (N=81) and shallower (R<20.1) sample of galaxies in ABGC 209, thus confirming that the R-band KR is invariant in the redshift range from z=0.023 to z=0.64. For what the K-band KR is concerned, our slope is fully consistent with that found by La Barbera et al. (2004) for the galaxies in the cluster A2163B at z~0.2.

The structural properties of early-type galaxies define a plane in the three-dimensional space (logr<sub>e</sub>, logn, <μ<sub>e</sub>>), the so-called PHP (see Graham 2002 and references therein):

$$\log r_e = a \log n + b <\mu_e> + c .$$

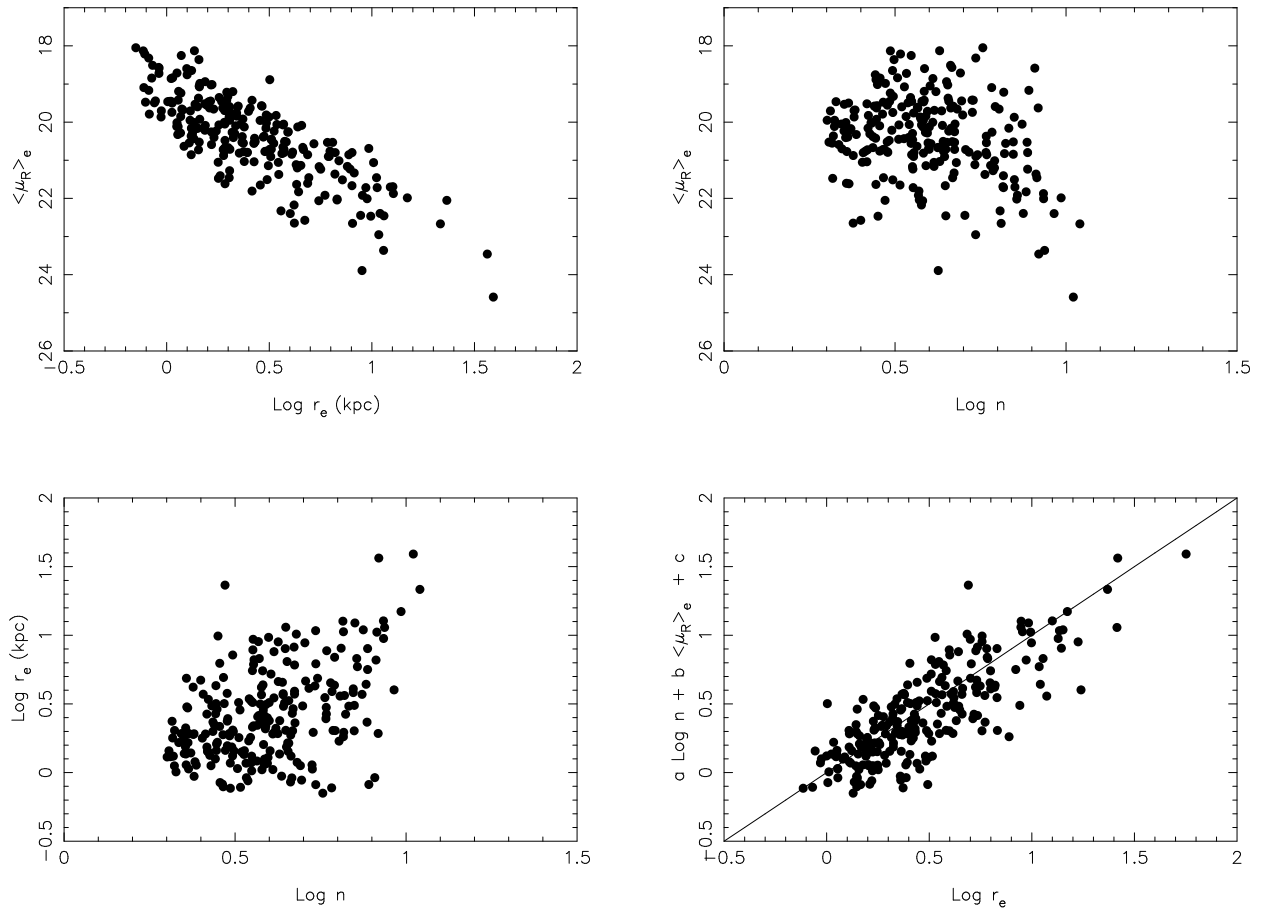
We derived coefficients of the PHP by using the corrected orthogonal weighted least-squares fit (La Barbera et al. 2005). This method, treating equally all the variables, gives much more robust estimates for the coefficients of the PHP and is less sensitive than others to selection effects.

The distribution of galaxies in the space of structural parameters is shown in Figs. 15 and 16, for R and K band respectively. We show the distribution of galaxies in the logr<sub>e</sub>-<μ<sub>e</sub>>, logn-<μ<sub>e</sub>> and logn-logr<sub>e</sub> planes, and an edge projection of the plane. Galaxies follow a well-defined PHP at z= 0.2, with Sersic indices that increase towards lower surface brightness values and larger effective radii.

In Table 4 we report the coefficient of the PHP for R and K band. The coefficients of the R- and K-band PHP are consistent (at 1σ) with those obtained by La Barbera et al.

**Table 4.** Coefficients of the PHP.

Band	a	b	c	$\sigma_{\log r_e}$
R	$0.964 \pm 0.130$	$0.209 \pm 0.020$	$-4.376 \pm 0.401$	$0.162 \pm 0.014$
K	$0.711 \pm 0.098$	$0.227 \pm 0.022$	$-3.871 \pm 0.404$	$0.167 \pm 0.016$

**Figure 15.** Photometric Plane of ABCG 209 in the R band. The upper panels and the lower-left panel show the  $\log r_e - <\mu_e>$ ,  $\log n - <\mu_e>$  and  $\log n - \log r_e$  projections of the PHP, respectively. The lower-right panel shows the edge-on view of the R-band Photometric Plane. The plots show the N= 240 galaxies of the R-band sample.

(2005) for the cluster MS 1008 at  $z \sim 0.3$  and by Graham et al. (2005) for nearby clusters, confirming that PHP seems to be independent of redshift.

### 6.3 The intrinsic dispersion of the PHP

In Table 4 we showed that the PHP has a small intrinsic dispersion ( $\sigma_{\log r_e} = 0.16 - 0.17$ ) both in R and K band. La Barbera et al. 2005 pointed out that stellar populations can be the origin of the dispersion about the plane. However they have shown that the residuals of the I-K versus K colour-magnitude relation do not correlate with the residuals about the PHP.

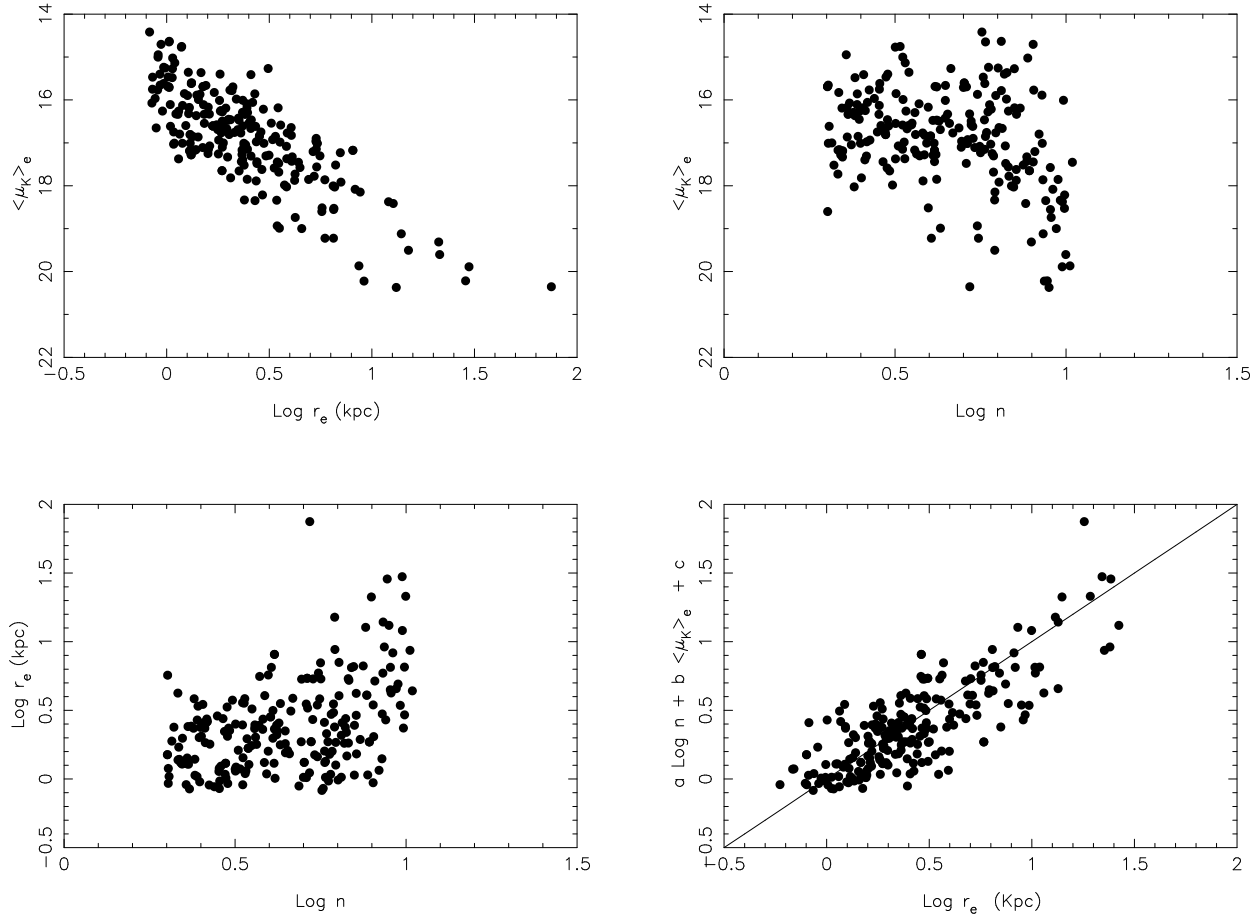


**Figure 16.** Photometric Plane of ABCG 209 in the K band. The upper panels and the lower-left panel show the  $\log r_e - \langle \mu_e \rangle$ ,  $\log n - \langle \mu_e \rangle$  and  $\log n - \log r_e$  projections of the PHP, respectively. The lower-right panel shows the edge-on view of the K-band Photometric Plane. The plots show the N= 227 galaxies of the K-band sample.

The dispersion about the PHP could be due to the combined effect of age, metallicity, and also  $\alpha/\text{Fe}$  enhancement, that cannot be distinguished only with the colour-magnitude relation. For this reason it is crucial to use line strength to address this issue.

In order to distinguish between the contribution of age, metallicity and  $\alpha/\text{Fe}$  enhancement, we compared the line indices obtained in Mercurio et al. (2004) with the residuals of PHP. We analyse a subsample of 83 and 91 ETGs, in R and K band respectively, for which we have these measurements. In particular we use  $H_\beta$ ,  $[\text{MgFe}]'$  (Thomas et al. 1986) and  $\text{Mgb}/\langle \text{Fe} \rangle$ , as the best indicators of age, metallicity and  $\alpha/\text{Fe}$  enhancement, respectively (see also Puzia et al. 2005).

Figure 17 shows that the  $H_\beta$  (upper panel) and  $[\text{MgFe}]'$  indices (central panel) do not correlate with either the R-band PHP (filled circles) or the K-band PHP (open circles). The dispersion of the PHP seems instead related to  $\text{Mgb}/\langle \text{Fe} \rangle$  measurements (lower panel).

We perform a least-square fit on the data, obtaining  $-0.051 \pm 0.461$  and  $-0.261 \pm 0.705$  for the age and metallicity correlation slopes, while for the  $\alpha/\text{Fe}$  we obtain  $0.702 \pm 0.258$ .

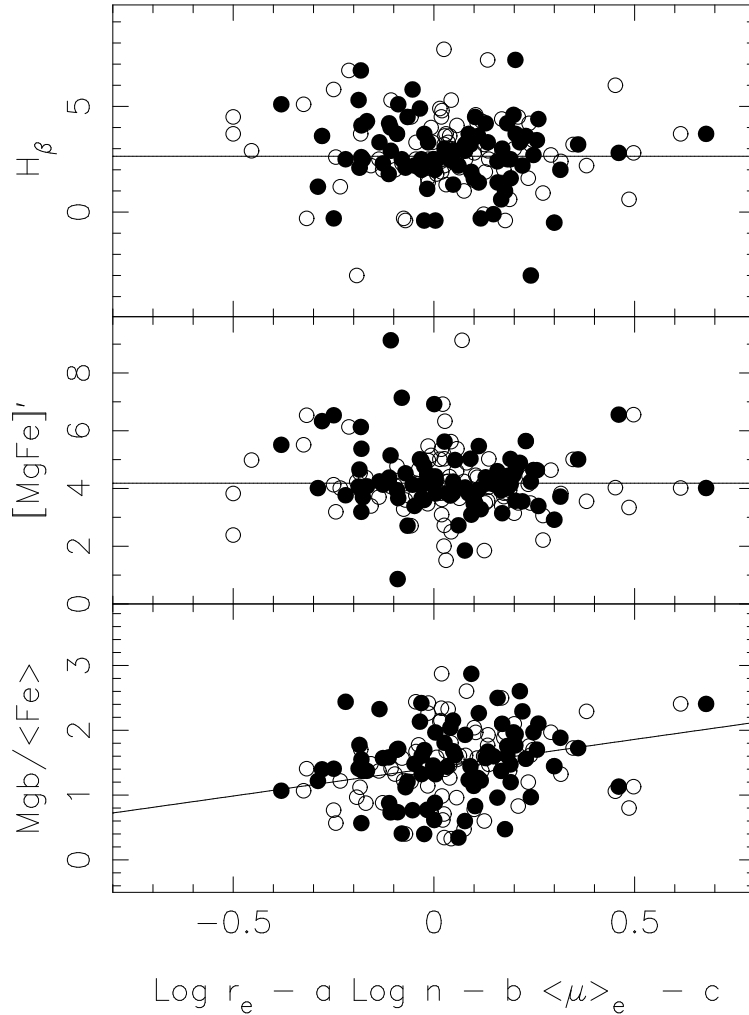


**Figure 17.** Correlation between PHP residuals and equivalent width of the  $H_\beta$  (upper panel), strength of  $[\text{MgFe}]'$  (central panel) and  $Mgb/\langle \text{Fe} \rangle$  (lower panel) for R (filled circles) and K (open circles) band. Continuous lines represent the least-square fit on the data.

This suggest that the chemical evolution of galaxies could be responsible for the intrinsic dispersion of the PHP, as argued by La Barbera et al. (2005).

## 7 SUMMARY AND CONCLUSIONS

In order to study the internal dynamics of the rich galaxy cluster ABCG 209, we have analysed spectra for a total sample of 148 galaxies in the cluster region, of which 134 are candidate cluster members having  $z \sim 0.209$ . In a previous paper we investigated the dynamical status of this cluster, selecting 112 galaxies belonging to the cluster (Mercurio et al. 2003a). We complement the previously described dataset with medium resolution spectra for 29 new cluster galaxies. We also re-observe 22 cluster members contained in the already available data sets. The enlarged data sets allow us to better distinguish among galaxies

belonging to different substructures, to derive their individual velocity distributions and to study possible spatial segregation.

We extend the existing optical ( $B$ ,  $V$  and  $R$  bands) photometry with  $K$ -band observations which allow us to estimate reliable photometric redshifts ( $\delta z/1 + z \leq 0.07$ ) for 399 galaxies brighter than  $R=21$  mag in the cluster field and to derive the NIR LF.

The Schechter function provides a good description of cluster galaxy counts, with  $\alpha = -0.98 \pm 0.15$  and  $K^* = 14.80 \pm 0.30$  mag, values consistent with previous studies of NIR luminosity functions of cluster galaxies at  $z \sim 0.2$  (de Propris et al. 1998, Andreon & Pellò 2000, La Barbera et al. 2004). The only magnitude bin showing a larger deviation is that at  $K = 17.5$  mag, where a marginal ( $\sim 1.5\sigma$  significant) deficiency of cluster galaxies is found, that corresponds to the magnitude bin ( $20 < R < 21$  mag) where Mercurio et al. (2003b) find some indication of a dip in the optical luminosity functions of ABCG 209.

ABCG 209 is characterised by a very high value of the LOSVD:  $\sigma_v = 1268^{+93}_{-84}$  km s $^{-1}$ , that results in a virial mass of  $M_{vir} = 2.95^{+0.80}_{-0.78} \times 10^{15} h_{70}^{-1}$  M $_{\odot}$  within  $R_{vir} = 3.42 h_{70}^{-1}$  Mpc. The analysis of the velocity dispersion profile shows that such a high value of  $\sigma_v$  is already reached in the central cluster region suggesting the possibility that a mixture of clumps at different mean velocities causes the high value of the velocity dispersion and the virial mass. In fact, we found that a mixture of three Gaussians is the best description of the velocity distribution (at 98.4% c.l.). Assigning the member galaxies to individual groups we found the main clump ( $n_{gal}=102$ ) at mean redshift  $z = 0.2090$  with a velocity dispersion of  $\sigma_v = 847^{+52}_{-49}$  km s $^{-1}$  and other two groups of 16 galaxies each at  $z = 0.1988$  and  $z = 0.2172$  with  $\sigma_v = 323^{+47}_{-58}$  km s $^{-1}$  and  $\sigma_v = 289^{+57}_{-54}$  km s $^{-1}$  respectively.

This observational scenario confirms that ABCG 209 is presently undergoing strong dynamical evolution with the merging of two or more subclumps, in agreement with the recent detection of a radio halo (Giovannini et al. 2006). On the other hand, there are discrepancies between the dynamical, X-ray and lensing analyses. While Smith et al. (2005) and Zhang et al. (2007) found no evidence for multimodality in the dark matter distribution and subclumps in the XMM data respectively, an irregular X-ray morphology was identified by Rizza et al. (1998) in ROSAT data and by Mercurio et al. 2003a (see their Fig. 13) and Smith et al. 2005 (see their Fig. 6) in Chandra observations. In particular, the Mercurio et al. (2003a) analysis recognised two significant substructures. The principal one centred on the cD galaxy and the second about 50'' East of the cD, this secondary clump being coincident with the Eastern clump detected by Rizza et al. (1998). Since these two detected clumps are

close to each other, probably the absence of evident subclumps in the XMM-Newton data is due to the limited spatial resolution of this instrument.

Smith et al. (2005) suggest that this discrepancy could be related to time evolution and that sufficient time has elapsed after the merger. However, as also pointed out by Smith et al. (2005), numerical simulations suggest that both gas dynamics and substructure in the dark matter distribution may persist as long as  $\sim 5$  Gyr after a cluster merger, and that the relaxation time for these two matter components may be comparable. Moreover, the detection of a radio halo (Giovannini et al. 2006) supports a recent merging event. In fact numerical simulation indicate that the mergers could generate strong fluid turbulence, supplying energy to the electrons, which then radiate in the interstellar medium of radio halos, but the time during which the process is effective is  $\sim 10^8$  yr (Feretti 2007).

In independent lensing analyses of the optical CFHT images, Paulin-Henriksson et al. (2007) and Bardeau et al. (2007) measured virial masses of  $M_{200} = 7.7^{+4.3}_{-2.7} \times 10^{14} h_{70}^{-1} M_\odot$  and  $M_{200} = 7.2 \pm 2.0 \times 10^{14} h_{70}^{-1} M_\odot$  and scaled velocity dispersions  $\sigma_v = 924 \pm 84 \text{ km s}^{-1}$  and  $\sigma_v = 813 \pm 70 \text{ km s}^{-1}$  respectively, which are consistent with the value obtained for the main clump from the dynamical analysis. For this reason we suggest that the observed weak lensing masses are associated with the dark matter halo of the most prominent clump of ABCG 209. The clumps are not spatially segregated so they would not be separable in the dark matter maps which measure only the projected mass distribution, and the combined contribution of the secondary clumps is expected to be much lower than that from the primary one.

We have derived structural parameters of galaxies in the R and K bands in order to obtain the Kormendy relation and the Photometric Plane for ABCG 209, based on a total sample of 240 and 227 spheroids in optical and NIR, respectively. Spheroids define a tight sequence in the plane of the effective parameters with a slope  $\beta \sim 3$  in both bands. This slope of the KR is fully consistent with that derived in La Barbera et al. (2003b) for a smaller ( $N=81$ ) and shallower ( $R < 20.1$ ) sample of galaxies in ABGC 209, thus confirming that the R-band KR is invariant in the redshift range from  $z=0.023$  to  $z=0.64$ . For what the K-band KR is concerned, our slope is fully consistent with that found by La Barbera et al. (2004) for the galaxies in the cluster A2163B at  $z \sim 0.2$ .

The cluster ETGs at  $z \sim 0.2$  follow a tight correlation among  $\log r_e$ ,  $\langle \mu \rangle_e$  and  $\log n$ , with an intrinsic dispersion of  $\sim 0.17$  dex in both optical and NIR wavebands. This dispersion

is fully consistent with that found by La Barbera et al. (2005) for the cluster MS1008 at  $z \sim 0.3$  and Graham (2002) for ETGs in nearby clusters.

In order to investigate the origin of the intrinsic scatter of the PHP we have analysed the PHP residuals versus line-strength indices. We compare the line indices obtained in Mercurio et al. (2004) with the PHP residuals of member galaxies for a subsample of 83 and 91 ETGs, in R and K band respectively. In particular we use  $H_{\beta}$ ,  $[\text{Mg}/\text{Fe}]'$  (Thomas et al. 1986) and  $\text{Mgb}/<\text{Fe}>$ , as the best indicators of age, metallicity and  $\alpha/\text{Fe}$  enhancement, respectively (Thomas et al. 1986, Puzia et al. 2005). The PHP residuals do not correlate with age and metallicity, while there is a correlation with  $\alpha/\text{Fe}$  enhancement (Fig. 17). This could imply that the scatter of the PHP is due to variations in stellar population parameters, in particular it could be due to variations in the chemical evolution of early-type galaxies brought about by their merging histories.

## ACKNOWLEDGMENTS

AM is funded by the INAF-OAC.

## REFERENCES

- Abell G. O., Corwin H. G. Jr., Olowin R. P., 1989, ApJS, 70, 1
- Andreon S., Pelló R., 2000, A&A, 353, 479
- Akritas M. G., Bershady M. A., 1996, ApJ, 470, 706
- Ashman K. M., Bird C. M., Zepf S. E., 1994, AJ, 108, 2348
- Bardeau S., Soucail G., Kneib J. P., et al., 2007, A&A, 470, 449
- Bardelli S., Zucca E., Vettolani G., et al., 1994, MNRAS, 267, 665
- Beers T. C., Flynn K., Gebhardt K., 1990, AJ, 100, 32
- Beers T. C., Forman W., Hulchra J. P., Jones C., Gebhardt K., 1991, AJ, 102, 1581
- Bertin E., Arnouts S., 1996, A&AS, 117, 393
- Bekki K., 1999, ApJ, 510, L15
- Boschin W., Girardi M., Spolaor M., Barrena R., 2006, A&A, 449, 461
- Bruzual G., Charlot S., 2003, MNRAS, 344, 1000
- Busarello G., Merluzzi P., La Barbera F., Massarotti M., Capaccioli M., 2002, A&A, 389,
- Cardelli J. A., Clayton G. C., Mathis J. S., 1989, ApJ, 345, 245

- Carlberg R. G., Yee H. K. C., Ellingson E., et al., 1997, ApJ, 476, L7
- Clowe D., Gonzales A., Markevitch M., 2004, ApJ, 604, 596
- Colberg J. M., White S. D. M., Jenkins A., Pearce F. R., 1999, MNRAS, 308, 593
- Danese L., De Zotti C., di Tullio G., 1980, A&A, 82, 322
- de Propris R., Eisenhardt P. R., Stanford S. A., Dickinson M., 1998, ApJ, 503, 45
- de Propris R., Stanford S. A., Eisenhardt P. R., Dickinson M., Elston R., 1999, AJ, 118, 719 (dPS99)
- Diaferio A., Kauffmann G., Balogh M. L., et al., 2001, MNRAS, 323, 999
- Dressler A., Shectman S.A., 1988, AJ, 95, 985
- Ebeling H., Voges W., Böhringer H., et al., 1996, MNRAS, 281, 799
- Fadda D., Girardi M., Giuricin G., Mardirossian F., Mezzetti M., 1996, ApJ, 473, 670
- Fasano G., Franceschini A., 1987, MNRAS, 225, 155
- Feretti L., 2002, The Universe at Low Radio Frequencies, Proceedings of IAU Symposium 199, held 30 Nov.-4 Dec. 1999, Pune, India, ed. A. Pramesh Rao, G. Swarup, Gopal-Krishna, 133
- Feretti L., 2007, invited talk, to appear in the proceedings of the XLIst Rencontres de Moriond, XXVIth Astrophysics Moriond Meeting: "From dark halos to light", L.Tresse, S. Maurogordato and J. Tran Thanh Van, astro-ph/0612185
- Gavazzi G., Pierini D., Boselli A., 1996, A&A, 312, 397
- Giovannini G., Tordi M., Feretti L., 1999, New Astronomy, 4, 141
- Giovannini G., Feretti L., Govoni F., Murgia M., Pizzo R., Astr. Nach., Vol.327, Issue 5/6, p.563
- Girardi M., Fadda D., Giuricin G., et al., 1996, ApJ, 457, 61
- Girardi M., Giuricin G., Mardirossian F., Mezzetti M., Boschin W., 1998, ApJ, 505, 74
- Girardi M., Mezzetti M., 2001, ApJ, 548, 79
- Girardi M., Boschin W., Barrena R., 2006, A&A, 455, 45
- Graham A., 2002, MNRAS, 334, 859
- Haines C. P., Mercurio A., Merluzzi P., et al., 2004, A&A, 425, 783
- Huang J. S., Thompson D., Kümmel M.W., et al., 2001, A&A, 368, 787
- Kennicutt R. C., 1992, ApJS, 79, 225
- Kormendy J., 1977, ApJ, 218, 333
- La Barbera F., Busarello G., Merluzzi P., Massarotti M., 2002, ApJ, 571, 790
- La Barbera F., Busarello G., Massarotti M., Merluzzi P., Mercurio A., 2003a, A&A, 409,

- La Barbera F., Busarello G., Merluzzi P., Massarotti M., Capaccioli M., 2003b, ApJ, 595, 127;
- La Barbera F., Merluzzi P., Iovino A., Massarotti M., Busarello G., 2003c, A&A, 399, 899;
- La Barbera F., Merluzzi P., Busarello G., Massarotti M., Mercurio A., 2004, A&A, 425, 797 (LM04)
- La Barbera F., Covone, G., Busarello G., et al., 2005, MNRAS, 358, 1116
- La Barbera F., et al., 2008, SPIE, in press
- Limber D. N., Matheus W. G., 1960, ApJ, 132, 286
- Malumuth E. M., Kriss G. A., Van Dyke Dixon W., Ferguson H. C., Ritchie C., 1992, AJ, 104, 495
- Massarotti M., Iovino A., Buzzoni A., 2001a, A&A, 368, 74
- Massarotti M., Iovino A., Buzzoni A., Valls-Gabaud D., 2001b, A&A, 380, 425
- Mercurio A., Girardi M., Boschin W., Merluzzi P., Busarello G., 2003a, A&A, 397, 431
- Mercurio A., Massarotti M., Merluzzi P., et al., 2003b, A&A, 408, 57
- Mercurio A., Busarello G., Merluzzi P., et al., 2004, A&A, 424, 79
- Merluzzi P., Busarello G., Massarotti M., La Barbera F., 2002, proceedings of the ASP Conference Tracing Cosmic Evolution with Galaxy Clusters, Vol. 268. Edited by Stefano Borgani, Marino Mezzetti, and Riccardo Valdarnini. ISBN: 1-58381-108-7 San Francisco, Astronomical Society of the Pacific, 2002., p.413
- Merluzzi P., La Barbera F., Massarotti M., Busarello G., Capaccioli M., 2003, ApJ, 589, 147
- Moss C., 2006, MNRAS, 373, 167
- Paulin-Henriksson S., Antonuccio-Delogu V., Haines C. P., Radovich M., Mercurio A., Becciani U., 2007 A&A, 467, 427
- Persson S. E., Murphy D. C., Krzeminski W., Roth M., Rieke M. J., 1998, AJ, 116, 2475
- Pisani A., 1993, MNRAS, 265, 706
- Press W. H., Teukolsky S. A., Vetterling W. T., Flannery B. P., 1992, in Numerical Recipes (Second Edition), Cambridge University Press
- Puzia T. H., Kissler-Patig M., Thomas D., et al., 2005, A&A, 439, 997
- Quintana H., Carrasco E. R., Reisenegger A., 2000 AJ, 120, 511
- Rizza E., Burns J. O., Ledlow M. J., et al., 1998, MNRAS, 301, 328
- Saglia, R. P., Bertschinger, E., Bagley, G., 1997, ApJS, 109, 79

- Schlegel D., Finkbeiner D. P., Davis M., 1998, ApJ, 500, 525 (SFD98)
- Smith G. P., Kneib J. P., Smail I., et al., 2005, MNRAS, 359, 417
- The L. S., White S. D. M., 1986, AJ, 92, 1248
- Thomas D., Maraston C., Bender R., 2003, MNRAS, 339, 897
- Tonry J., Davis M., 1981, ApJ, 1511
- van Dokkum P. G., Franx M., Kelson D. D., Illingworth G. D., 1998, ApJL, 504, 17
- Zhang Y. Y., Finoguenov A., Boehringer H., et al., 2007, A&A, 467, 437
- Ziegler B. L., Saglia R. P., Bender R., et al., 1999, A&A, 346, 13